

Volume 3 Issue 1 December 2020 ISSN 2635-4608

# Journal of Medical Imaging






**VOL. 3**



**AIMS OF THE JOURNAL**

The scope of the ScholarGen Journal of Medical Imaging (SJMI) is all about medical imaging. The SJMI publishes medical imaging theories, methods, systems and data collection, image reconstruction and image analysis. Also, SJMI covers related research fields for cell and molecular level imaging for early detection and diagnosis of disease.

<b>SCOPE OF THE JOURNAL</b>	<b>JOURNAL HIGHLIGHT</b>	<b>Indexing</b>
Radiography MRI Nuclear medicine Ultrasound Thermography Molecular Imaging NMR in Biomedicine Software, Tools Other studies on radiology	Radiography Magnetic Resonance Imaging Nuclear medicine Ultrasound Thermography Molecular Imaging NMR in Biomedicine Software, Tools Other studies on radiology	  

**Open Access Journals by scholargen publisher is licensed under a Creative Commons Attribution-NonCommercial 4.0 International License.**

4-17-27 Tenjin-cho, Kodaira, Tokyo, Japan  
 Email : info@scholargen.com  
 Scholargen International Cooperation

Pirogov St., 630090, Novosibirsk, Russia  
 35B, Pocket B, Siddhartha Extn, New Delhi  
 Private Bag X3, Rondebosch 7701, Cape Town  
 75, Nowon-ro, Nowon-gu, Seoul, Korea  
 Sydney, New South Wales 2052, Australia  
 Valikhovsky Lane 2, Odessa, 65028, Ukraine  
 Venezuela, Santa Cruz de la Sierra, Bolivia  
 2329 West Mall Vancouver, BC, Canada  
 Spui 21, 1012 WX Amsterdam, Netherlands



# Journal of Medical Imaging

<b>Content</b>	<b>ISSN 2635-4608</b>	<b>j. med. Imaging(ScholarGen) Volume 3, Issue 1, December 2020</b>
----------------	-----------------------	---

1. *Magnetic Nanoclusters for T2 MR Imaging in Cancer using Xenograft Mice Model*-----  
----- Jooyeon Kim, GilJae Lee, Jingyu Kim
11. *Analysis of Changes in Signal Intensity of Choroidal Plexus in MRI Using FLAIR-DW-EPI Pulse Sequence* -----Jingyu Kim, Sang-Jin Im
17. *Determining the Degree of Malignancy on Digital Mammograms by Artificial Intelligence Deep Learning* -----Sang-Bock Lee, 2Hwunjae Lee, V. R. singh
33. *Peak Signal-to-Noise Ratio Evaluation of Server Display Monitors and Client Display Monitors in a Digital Subtraction Angiography Devices* -----Hwunjae Lee, Junhaeng Lee
43. *Analysis of Fitting Degree of MRI and PET Images in Simultaneous MR<sub>1</sub>PET Images by Machine Learning Neural Networks*----- GilJae Lee, Hwunjae Lee, Gyehwan Jin

# Magnetic Nanoclusters for T2 MR Imaging in Cancer using Xenograft Mice Model

<sup>1</sup>Jooyeon Kim, <sup>2\*</sup>GilJae Lee, <sup>3</sup>Jingyu Kim

Received : 25 August 2020 / Accepted : 30 November 2020 / Published online : 28 December 2020

©The Author(s) 2020

**Abstract** In this study, we tried to develop nanoprobe for molecular magnetic resonance (MR) imaging using magnetic nanoclusters (MNC). MNCs for magnetic resonance imaging were synthesized by thermal decomposition.

The size of the synthesized MNC was confirmed to be  $73 \pm 32.4$  nm. Cytotoxicity test of the synthesized MNCs showed that the cell state of about 80% or more did not change in all the treatment ranges and cell survival rate was high even though the MNCs were injected. MNC was injected intravenously into the tail vein of nude mice.

As a result, it was found that enhancement of the contrast was confirmed in xenograft mice model using MNC. These results will contribute to clinical application and related research through magnetic nanocluster in the future.

Key-word : MR Molecular Imaging, magnetic, Chemical exchange saturation transfer (CEST), Nanoclusters (MNC), Magnetic nanoparticles (MNPs)

## 1. INTRODUCTION

Molecular imaging is a technique for diagnosing various changes at the cellular level. It is a field where advanced imaging technology and molecular cell biology are combined and has recently developed rapidly through a fusion of medicine, genetics, molecular biology, cytology, chemistry, pharmacology, physics, biomedical engineering, radiology, and nuclear medicine.

The imaging technologies and devices used in molecular imaging are Single Photon Emission Computed Tomography (SPECT), Positron Emission Tomography (PET), Magnetic Resonance Imaging (MRI), Ultrasonography, Fluorescence, and Bioluminescence. Molecular imaging has used for early diagnosis of cancer, new drug development,

---

<sup>1</sup>Jooyeon Kim e-mail : jooyun8992@kbsi.re.kr  
Department of Research Equipment Operation  
Korea Basic Science Institute, Cheong-won, Ochang,  
Republic of Korea

<sup>2\*</sup>GilJae Lee (✉) **corresponding author**  
Business Promotion Agency, Chungbuk Technopark  
(28116)40, Yeongudanji-ro, Cheongju-si,  
Chungcheongbuk-do, Korea

<sup>3</sup>Jingyu Kim  
Dept. of Radiological & Madico-Oncological Science,  
University of Science & Technology  
(34113) 217, Gajeong-ro, Yuseong-gu, Daejeon, Korea  
e-mail : [jingyu8754@kirams.re.kr](mailto:jingyu8754@kirams.re.kr)

gene therapy, stem cell research and treatment, and disease prognosis prediction[1]. MR molecular imaging can be performed noninvasively without radiation exposure. In addition, MR molecular imaging has excellent safety and image quality. Recently, chemical exchange saturation transfer (CEST), magnetic nanoparticles (MNPs) and magnetic nano clusters (MNCs) Research are being actively carried out.

MNCs are structures in which nanoparticles of 1 to 100 nanometers (10 to - 9 meters) in diameters, such as MNPs, gold nanoparticles, and quantum dots, are assembled. This structure has unique collective properties that are different from single nanoparticles. The MNCs showed a  $T_2$  relaxation rate three times higher than that of the conventional MR imaging contrast agent Feridex and was well transferred to specific cells.

These results demonstrate that MNPs can be used in biomedical and medical applications such as MR molecular imaging, fluorescence imaging, and drug delivery [2].

This study is to develop a novel nanoprobe for MR molecular imaging of gastric cancer using MNCs based on MNPs which can be used for MR molecular imaging.

## 2. EXPERIMENTAL METHODS

### 2.1. Materials

Polysorbate, ethylenediamine, 1,4-dioxane, 4-dimethylamino-pyridine, triethylamine, and succinic anhydride(SA) were purchased from Sigma Aldrich Chemical Co. Phosphate buffered saline (PBS: 10 mM, pH 7.4) were purchased from Roswell Park Memorial Institute, and antibiotic-antimycotic solution Dialysis membrane was used. The gastric cancer cell line (American type culture collection) was incubated in an incubator containing fetal bovine

serum and antibiotic antimycotic. Ultra pure deionized water was used for all synthesis.

### 2.2. Synthesis of Magnetic Nano Cluster

MNC was synthesized by the nanoemulsion method. The nanoemulsion process was carried out by following the two-step synthetic procedure. First, monocrystalline manganese iron nanoparticles are synthesized by pyrolysis from non-polar inorganic solvent to metal-inorganic precursors, and synthesized manganese iron is synthesized by seed-mediated growth method.

### 2.3. MNC Cytotoxicity Test

The gastric cancer cell line was cultured under the conditions of RPMI medium and antibiotics, and various concentrations of MNCs were treated for 4 hours. The cytotoxicity test of MNC on gastric cancer cell line was performed by measuring 3-(4,5-dimethyl-thiazole-2-yl) -2,5-diphenyltetrazolium bromide (MTT) assay.

### 2.4 Zenograft animal models and experimental procedures

All animal studies were approved and accredited by the Association for Assessment and Accreditation of Laboratory Animal Care (AAALAC) International. Six-week-old female nude mice were injected intravenously with an anesthetic Zoletyl / Rompun mixture. After anesthesia,  $1.0 \times 10^7$  gastric cancer cell lines were dispersed in 200 mL saline solution and injected into the thighs of mice. MR images were obtained at 5th week after transplantation of gastric cancer cell line.

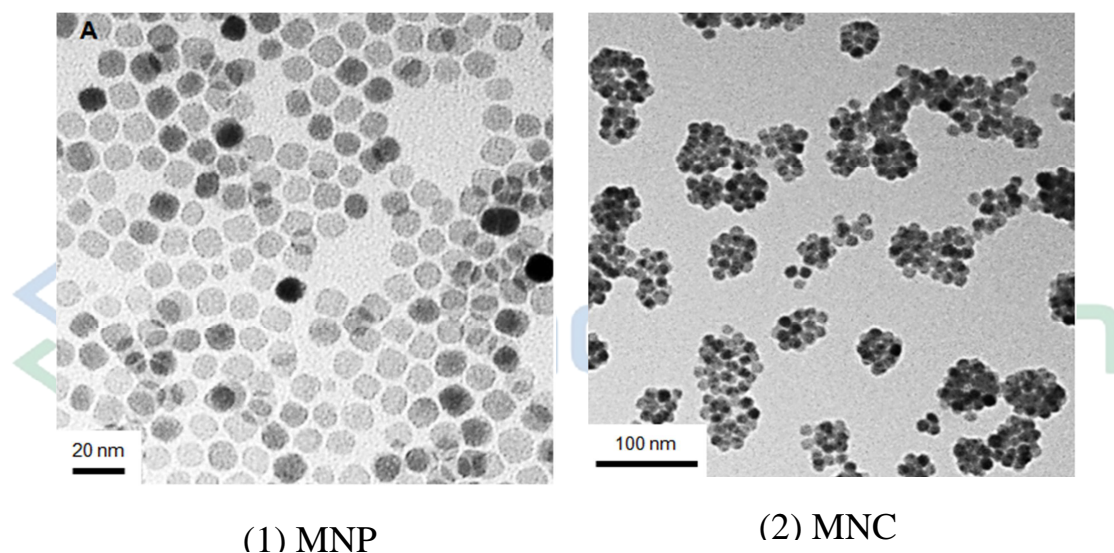
### 2.3 MR Imaging

Animal solution MRI was performed with 3 T Phillips clinical MRI equipment and T<sub>2</sub> weighted images were obtained using wrist coils. The conditions for obtaining T<sub>2</sub>-weighted images were TR (repetition time): 700.85 ms, TE (echo time): 100.65 ms, Slice thickness: 1.0 mm, and FOV read: 100 mm.

### 3. RESULT & DISCUSSION

#### 3.1. MNCs Characteristics

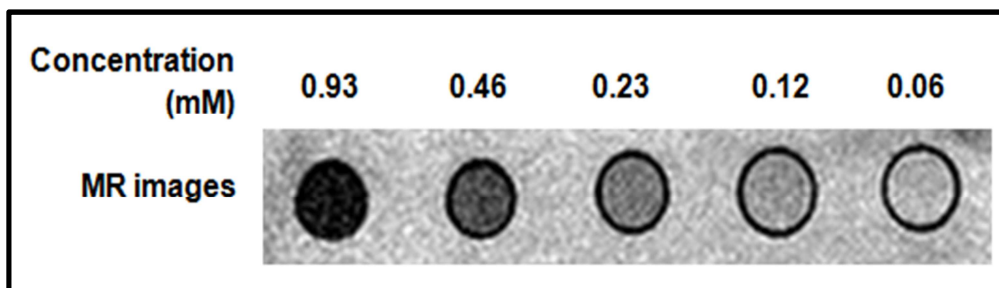
MNCs for MR contrast agents were synthesized by thermal decomposition methods. The manganese iron in the inorganic state was combined with PLI (Poly-L-Lysine) by emulsion method, and the remaining PLI was removed using Centrifuge and MNCs were synthesized with proper PLI ratio. As shown in [Figure 1], transmission electron microscope (TEM) was used to confirm the size distribution and morphology of MNCs. TEM confirmed that the size of the MNCs was  $73 \pm 32.4$  nm.



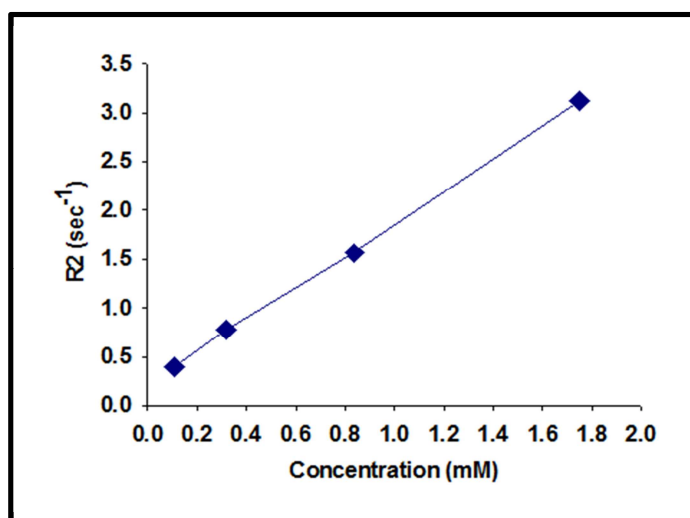
[Figure 1] TEM imaging of MNP and MNC

MRI was performed to confirm the characteristics of the synthesized cluster as a MRI contrast agent. Appropriate-sized clusters could adequately avoid the reticuloendothelial system (RES), allowing them to stay longer in the blood.

As shown in [Figure 2], T<sub>2</sub> images according to cluster concentration were confirmed through MRI, and it was confirmed that the T<sub>2</sub> value was increased with increasing concentration as shown in [Figure 3].



[Figure 2] MNCs T2 imaging

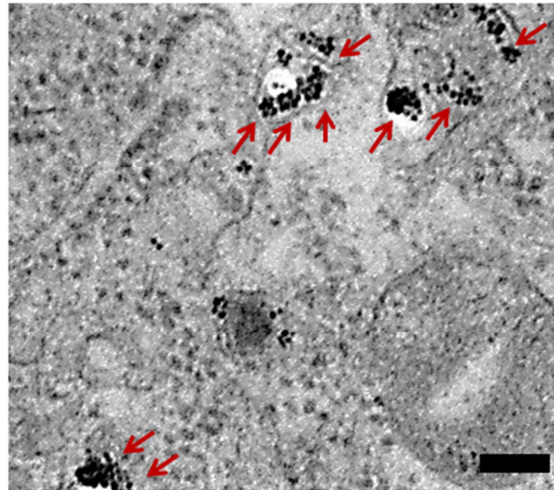
[Figure 3] R<sub>2</sub> relaxation rate with increasing MNCs concentration

### 3.2. MNC cytotoxicity test

Cytotoxicity tests should be carried out to determine the side effects of drugs intended to be injected into the living body including the contrast agent. Although there are objections to the sacrifice of animals, experiments through simulations have not been fully validated to date. Animal experiments are performed to reproduce the target concentration changes and effects of experimental cell lines during ADME (administration, distribution, metabolism, and emission) processes and processes in vivo with high accuracy.

In this study, cell growth retardation was examined using animal experimental cell lines. We investigated normal cell damage and normal cell function after injection of MNCs contrast agent.

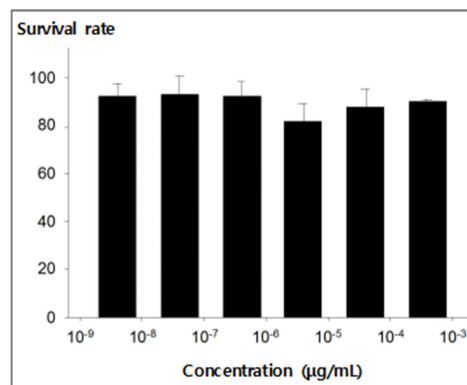
To evaluate cytotoxicity, 3-(4,5-dimethylthiazol-2-yl) -2,5-diphenyltetrazolium bromide (MTT) test was performed on gastric cancer cell line. The gastric cancer cell line was treated with NMCs synthesized in the range of  $10^{-7}$  to  $10^{-1}$  and cultured for 24 hours. [Figure 4] shows the appearance of particle-type MNPs contrast agent and clustered MNCs contrast agent.



[Figure 4] MNCs MNC-74 cells (scale bar: 100 nm) – TEM image

In all treatments of synthesized NMCs, no more than 80% of the cell states were changed. As shown in [Figure 5], cell survival rate was high even though

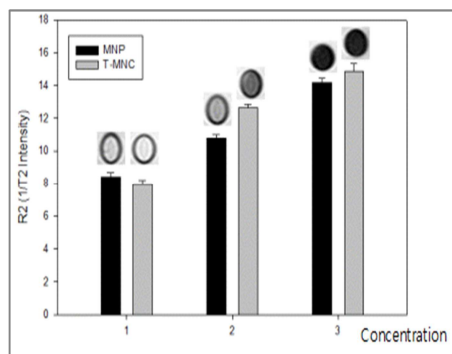
MNCs was injected. As a result, there was no cytotoxicity of newly synthesized MNCs.



[Figure 5] Toxicity test results of MNC cells

[Figure 6] shows the evaluation of the degree of contrast enhancement by administering MNPs (black graph) contrast agent and clustered MNCs (gray graph) contrast agent to the cells, respectively. Comparisons of contrast enhancement after

administration of the two contrast agents at the same concentration showed that the enhanced contrast enhancement effect of the clustered MNCs contrast agent was greater.



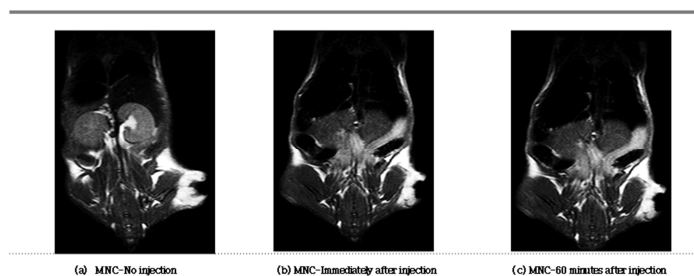
[Figure 6] Contrast enhancement of MNP and MNC

### 3.3. In vivo MRI

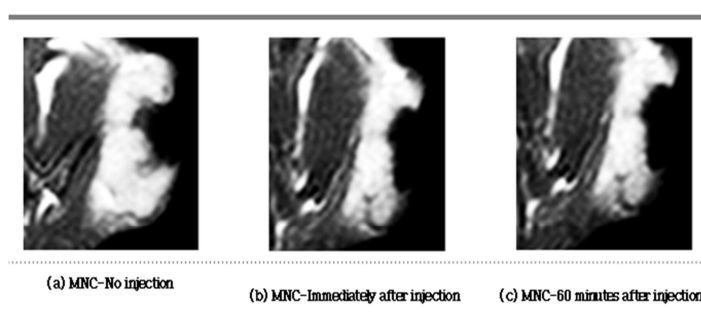
An animal model in which a gastric cancer cell line was transplanted into the thigh of a nude mouse was established. MRI was acquired using a  $T_2$  pulse sequence after injecting the synthesized MNCs into the tail vein of a mouse. The intravenous injection into the tail vein of the nude mouse and observation of the passage of time showed that the grafted cancer

cell site was specifically stressed. As shown in [Figure 7] and [Figure 8], non-MNCs images and MNCs images of cancer were acquired over time.

Over time, it was confirmed that the blood vessels in the periphery of the gastric cancer cell line were enhanced. As a result, it was found that the newly synthesized MNCs were suitable for the role of the MR molecular imaging probe for the early diagnosis of cancer.



[Figure 7] Comparison of non-MNCs image and MNCs images



[Figure 8] Comparison between non-MNCs and MNCs images (ROI)



#### 4. CONCLUSION

In this study, we developed molecular MR imaging nano cluster for early diagnosis of cancer.

We designed Magnetic Nanocluster is more efficient than conventional Magnetic nanoparticles in contrast enhancement issue. In addition, since magnetic nanocluster which consisting of numerous magnetic nanoparticles was synthesized with a biocompatible polymer, the toxicity issue was also resolved. In our future studies, pathological confirmation will also be required. Also, biocompatible Magnetic nanoclusters will be actively developed in clinical applications and related research.

#### Competing interests

The authors declare that there is no conflict of interest regarding the publication of this paper.

#### [REFERENCE]

- [1] Pack D. S, Choi G. R, Han B. S, & Ahn, B. J.,(2012). Feature values of DWT using MR general imaging and molecular imaging. *Journal of the Korean Society of Radiology*, 6(5), 409-414.
- [2] Nirbhay, Y.(2014). *Chemical Exchange Saturation Transfer(CEST) MRI : Theory and Applications*, University of Western Sydney Previous Nanoscale Research Seminars.
- [3] Mahwood U.(2003), *Emerging Technologies That Will Change the World*, *Molecular Imaging. Tech. Rev.*, 106.
- [4] Choi, G. R., & Lee, S. B.,(2014). *Application and Prospects of Molecular Imaging*. *J. Korean. Soc. Radiol.*, 8(3), 123-136.
- [5] Ha S.W.(2012). *Preparation and evaluation of ultrasuperparamagnetic iron oxide nanoparticle for MRI contrast agent*. Mater Thesis, University of Science and Technology.
- [6] Esserman, L., Wolverton, D., Hylton, N.(2002). *Magnetic resonance imaging for primary breast cancer management; current role and new applications*, *Endo. Rel. Cancer*. 9. 141.
- [7] A. Maiocchi.(2003). *The Use of Molecular Descriptors in the Design of Gadolinium(III) Chelates as MRI Contrast Agents*, *Mini Med. Chem*. 3. 845.
- [8] Wang, Y., Hussain, S., & Krestin, G.,(2001). *Superparamagnetic iron oxide contrast agents: physicochemical characteristics and applications in MR imaging*. *Eur. Radiol.*, 11(11). 2319-2331.
- [9] Nasongkla, N., Bey, E., Ren, J., Ai, H., Khemtong, C., Guthi, J. S., Chin, S. F. Sherry, A. D., Boothman, D. A. & Gao, J.,(2006). *Multifunctional Polymeric Micelles as Cancer-Targeted, MRI-Ultrasensitive Drug Delivery Systems*. *Nano Lett.*, 6(11). 2427-2430.
- [10] Tournier H, Hyacinthe R, Schneider M.,(2002). *Gadolinium-containing mixed micelle formulations: A new class of blood pool MRI/MRA contrast agents*. *Acad. Radiol*. 9. S20–S28.



## Analysis of Changes in Signal Intensity of Choroidal Plexus in MRI Using FLAIR-DW-EPI Pulse Sequence

<sup>1,\*</sup>Jingyu Kim, <sup>2</sup>Sang-Jin Im

Received : 25 June 2020 / Accepted : 15 October 2020 / Published online 28 December 2020

©The Author(s) 2020

**Abstract** In this study, the signal intensity of choroid plexus, which is producing cerebrospinal fluid, is analyzed according to the FLAIR diffusion-weighted imaging technique. In the T2\*-DW-EPI diffusion-weighted image, the FLAIR-DW-EPI technique, which suppressed the water signal, was additionally examined for subjects with high choroid plexus signals and compared and analyzed the signal intensity. As a result of the experiment, it was confirmed that the FLAIR-DW-EPI technique showed a signal strength equal to or lower than that of the brain parenchyma, and there was a difference in signal strength between the two techniques. As a result of this study, if the choroidal plexus signal is high in the T2\*-DW-EPI diffusion-weighted image, additional examination of the FLAIR-DW-EPI technique is thought to be useful in distinguishing functional problems of the choroid plexus. In conclusion, if the choroidal plexus signal is high on the T2\*-DW-EPI diffuse weighted image, it is thought that further examination of the FLAIR-DW-EPI technique will be useful in distinguishing functional problems of the choroidal plexus.

**Key-word** : Choroid plexuses, Diffusion weighted image, FLAIR, Signal intensity

---

<sup>1,\*</sup>Jingyu Kim (✉) *corresponding author*  
Dept. of Radiological & Madico-Oncological Science,  
University of Science & Technology  
(34113) 217, Gajeong-ro, Yuseong-gu, Daejeon, Korea

<sup>2</sup>Sang-Jin Im  
M.Sc. Biomedical Science Lee Gil Ya Cancer and Diabetes Institute,  
Gachon University  
(21999) 155, Gaetbeol-ro, Yeonsu-ku, Incheon, Korea

### I. Introduction

The diffusion-weighted image is an image of the degree of diffusion of water molecules in a tissue using an MR device<sup>[1]</sup>. The diffusion-weighted image is an image of the degree of diffusion of water molecules in a tissue using an MR device. In MRI, the diffusion of water molecules decreases the signal, so if the diffusion is good, the signal is weak, and if the diffusion is not good, the signal is strong. The clinical application of diffusion-weighted imaging is used for early diagnosis of acute cerebral infarction, differentiation between brain tumors and abscesses, and diagnosis of CJD (Creutzfeldt-Jakob Disease)<sup>[2]</sup>. Brain tissue is an aggregate of over 100 billion nerve cells, and the movement of water molecules is not completely free and is limited by the characteristics of the tissue. Isotropic diffusion refers to a case where water molecules can move in any direction, and anisotropic diffusion refers to a case where water molecules move in a specific direction only by surrounding structures<sup>[3]</sup>. Water molecules in the human brain tissue are not completely free, and in addition to the diffusion movement of fine water molecules, the movement of the brain tissue itself, cardiac movement, blood flow in the micro-vessel,

and movement of the patient are affected. The diffusion coefficient measured during actual MRI includes the effects of these various factors and is called the apparent diffusion coefficient (ADC)<sup>[4]</sup>. The degree of diffusion can be qualitatively predicted according to the signal intensity, and the diffusion coefficient can be calculated and analyzed quantitatively<sup>[5]</sup>. The choroid plexus or plica choroidea, is a plexus of cells that arises from the tela choroidea in each of the ventricles of the brain. The choroid plexus consists of modified ependymal cells surrounding a core of capillaries and loose connective tissue. There are many capillaries in the choroid layer, and consists of a window-shaped capillary and one layer of polar epithelial cells surrounding it, and is directly involved in the production of cerebrospinal fluid. The choroid plexus produces most of the cerebrospinal fluid (CSF) of the central nervous system. When the water permeability due to the difference in osmotic pressure of the choroidal plexus is significantly reduced, the production of cerebrospinal fluid is significantly reduced. MRI brain diffusion imaging has been helpful in the diagnosis and treatment of super-acute cerebral infarction in clinical practice<sup>[6]</sup>. In addition, it has been usefully used to differentiate between an arachnoid cyst and epidermoid cyst, and to diagnose brain abscess<sup>[7]</sup>. However, research on the fact that the signal intensity varies depending on the degree of diffusion according to the inspection technique of the diffusion-weighted image is not active<sup>[7]</sup>. In this study, the signal intensity of choroid plexus, which is producing cerebrospinal fluid, is analyzed according to the FLAIR diffusion-weighted imaging technique.

## II. Materials and methods

### 1. T1 and T2 weighted image

When performing an actual MRI, 90-degree high-frequency pulses usually have to be repeatedly applied

hundreds of times, so the time interval between pulses (repetition time, TR) has a great influence on the MRI signal. That is, if the TR is long, both tissues with a long T1 relaxation time or short tissues are subjected to the next 90-degree pulse while sufficiently recovering the longitudinal magnetization, and a strong signal can be generated every 90-degree pulse<sup>[8]</sup>. However, if the TR is short, the fat tissue with a short T1 relaxation time can sufficiently recover the longitudinal magnetization, but other tissues fail to recover sufficiently, and the next 90-degree pulse is applied. As a result, the MRI signal is reduced. Therefore, if the TR is shortened, an image that reflects the difference in T1 relaxation time between tissues as contrast can be created, and this is a T1 weighted image<sup>[8]</sup>. In other words, the T1 weighted image uses a short TR and a short TE, and a short TR enhances T1 contrast between tissues, and a short TE suppresses T2 contrast<sup>[8]</sup>.

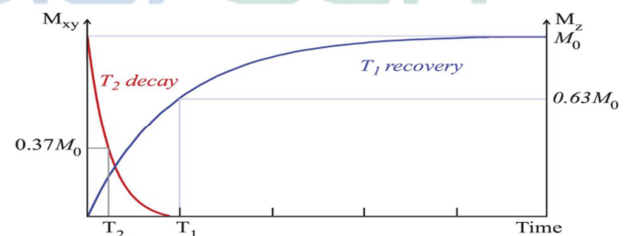


Figure 1. T1 relaxation and T2 decay<sup>[9]</sup>

The transverse magnetization created by the 90-degree high-frequency pulse decays with time. If a high-frequency pulse of 180 degrees is applied at an appropriate time, the vector of the transverse magnetization that is decaying is changed 180 degrees in the opposite direction, so that the transverse magnetization can be refocused. The time interval between the 90-degree pulse and the signal generation is called the echo time (TE), and by adjusting this, an

image reflecting the difference in T2 relaxation time between tissues as a contrast, that is, a T2 weighted image can be obtained. When TE is shortened and the transverse magnetization decay of the tissue does not occur, a 180-degree pulse is applied to obtain an image with low T2 contrast between tissues. On the other hand, when TE is lengthened and a 180-degree pulse is applied at a time when the T2 between tissues is sufficiently different, a T2 weighted image with high T2 contrast is obtained<sup>[10]</sup>.

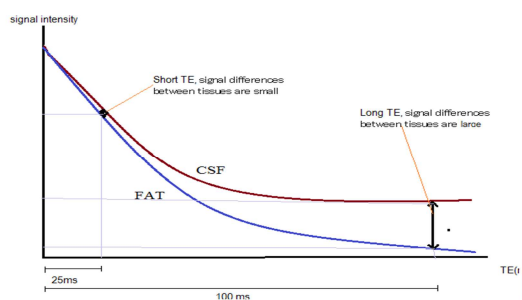


Figure 2. Signal difference between fat and water according to TE time<sup>[10]</sup>

## 2. FLAIR (fluid attenuated inversion recovery)

The FLAIR technique is a technique that suppresses the signals of the cerebrospinal fluid as a kind of inversion recovery technique<sup>[11]</sup>. The white matter-gray matter contrast is similar to that of the T2-weighted image, except that the signal of the cerebrospinal fluid is suppressed black because the long TR and the long TE are used. The sequence of pulses in the spin-echo image starts with a 90-degree pulse, but the inversion recovery technique applies a 180-

degree inversion pulse before the 90-degree pulse. Immediately after the 180-degree reversal pulse, the net magnetization of the tissue is completely inverted toward the (-) side of the longitudinal axis, and then T1 relaxation occurs according to the characteristics of each tissue, and magnetization in the (+) longitudinal direction begins to occur<sup>[11]</sup>. In this process, there is a point in time when the net magnetization of the vertical axis becomes zero, and the time from the 180-degree pulse to this point is called the inversion time (TI). Fat has a reversal time of 150 ms, white matter 300-400 ms, gray matter 600-700 ms, and cerebrospinal fluid 2000-2500 ms. Therefore, the 90-degree pulse is applied after waiting for the inversion time of the tissue to suppress the signal after the 180-degree inversion pulse<sup>[12]</sup>. That is, applying a 90-degree pulse after 150 ms becomes a STIR (short TI inversion recovery) technique that suppresses the fat signal, and applying a 90-degree pulse after 2000 to 2500 ms results in a FLAIR image that suppresses the cerebrospinal fluid signal. It can be seen that the signal of the desired tissue can be suppressed by adjusting the inversion time using 180-degree pulses of various inversion times while the TR and TE are fixed. FLAIR images can easily detect small lesions adjacent to the CSF space, and lesions with slightly increased T2 signals<sup>[13]</sup>.

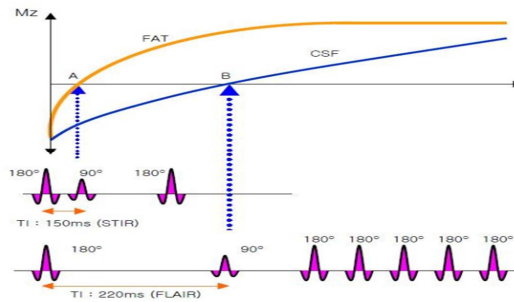


Figure 3. STIR and FLAIR according to TI<sup>[14]</sup>

**Table 1. Comparison of T2 weighted images and FLAIR images<sup>[15]</sup>**

	T2WI	FLAIR
<b>Normal image</b>		
<b>Embolic infractions</b>		
<b>Acute infraction</b>		

### III. Experimental

1.5 Tesla superconducting magnetic resonance imaging device and Head & Neck coil were used. We studied 17 patients (8 males and 9 females) with the high signal intensity of choroid plexus in diffuse-weighted imaging (T2\*-DW-EPI

technique). An image of a subject with high signal strength with choroid plexus was additionally obtained by applying the FLAIR-DW-EPI technique. The signal intensity and diffusion coefficient of choroid plexus were obtained and compared with the diffusion-weighted images obtained by the two techniques. The parameters for obtaining diffuse-weighted images were T2\*-DW-EPI and FLAIR-DW-EPI. Images were obtained using the same section of the same patient with a field of view of 28 cm, a section thickness of 6 mm, and a spacing of 1 mm. The T2\*-DW-EPI technique was set to repetition time (TR) 12,000 ms, echo time (TE) 160.0 ms, and inspection time 30 sec. The FLAIR-DW-EPI technique used repetition time (TR) 12,000 ms, echo time (TE) 140.0 ms, inversion time (TI) 2,400 ms, and test time 80 sec. In order to reduce magnetic susceptibility artifacts, the lateral ventricle posterior choroid plexus was observed from the skull base to the vertex in parallel to the glabellomeatal line. For image analysis, the image data was transmitted to the Workstation, and a region of interest (ROI) at the center of the choroid plexus was designated as 28 mm<sup>2</sup> to obtain signal intensity and diffusion coefficient. To compare the difference between the two techniques, the signal intensity and diffusion coefficient of acute cerebral infarction and intraventricular hemorrhage were calculated.

### IV. Result and Discussion

In the T2\*-DW-EPI technique, 19 patients showed the high signal intensity of the choroidal plexus. Of these, 10 were male and 9 were female. The average age of all of them was 61.3 years (33-89), the average age of men was 61.5 years, and the average age of women was 59.8 years. When comparing the images examined by applying the FLAIR-DW-EPI technique to those of the T2\*-DW-EPI technique, it was found that there is a significant difference in signal intensity.

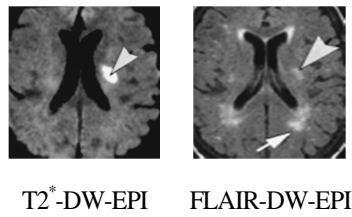


Figure 4. Choroid plexus

Quantitatively, in the T2\*-DW-EPI technique, the signal intensity of the choroid plexus was 251.6 mm<sup>2</sup>/s and the apparent diffusion coefficient (ADC) was 1.86×10<sup>3</sup> mm<sup>2</sup>/s. The FLAIR-DW-EPI technique was 61.3 mm<sup>2</sup>/s and the ADC was 1.84×10<sup>3</sup> mm<sup>2</sup>/s, which was similar to the brain cortex. The difference in signal intensity between the two techniques was 191 mm<sup>2</sup>, which was highly observed in the T2\*-DW-EPI technique, and there was little difference in the overt diffusion coefficient. In the case of acute cerebral infarction, both techniques showed high signal intensity and were 251.5 mm<sup>2</sup>/s and 212.8 mm<sup>2</sup>/s, respectively, and ADCs were 0.81×10<sup>3</sup> mm<sup>2</sup>/s and 0.80×10<sup>3</sup> mm<sup>2</sup>/s, respectively.

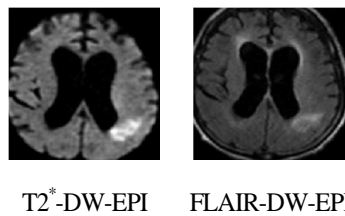


Figure 5. Acute cerebral infarction

**Table 2. Signal intensity analysis**

Label	DW-EPI	Signal intensity	ADC(X10 <sup>3</sup> )
Brain	T2*	116.1	1.08
	FLAIR	113.1	1.23
Choroid plexus	T2*	250.8	1.87
	FLAIR	60.8	1.85

Acute infraction	T2*	250.5	0.82
	FLAIR	212.6	0.80
Acute hemorrhage	T2*	389.4	0.84
	FLAIR	337.6	0.76

In the case of a lateral ventricular cerebral hemorrhage, both techniques showed high signal intensity, 389.6 mm<sup>2</sup>/s, and 337.8 mm<sup>2</sup>/s, respectively, and ADCs were 0.83×10<sup>3</sup> mm<sup>2</sup>/s and 0.77×10<sup>3</sup> mm<sup>2</sup>/s, respectively.

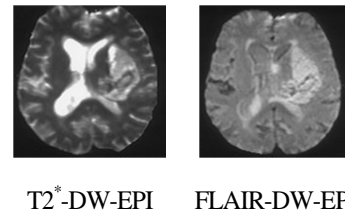


Figure 6. Lateral ventricular cerebral hemorrhage

The degree of signal attenuation by diffusion is proportional to the moving size of the molecule and the intensity of the diffusion-enhanced gradient magnetic field. The intensity of the diffusion-enhanced gradient magnetic field is called b-value (s/mm<sup>2</sup>), which is related to the intensity of the gradient magnetic field, the time applied to the gradient magnetic field, and the time interval between the front and rear gradient magnetic fields. In general, diffuse-enhanced images can be sufficiently visualized by applying a b value of about 1,000. In the diffusion-weighted image, the signal intensity is determined by the combination of the overt diffusion coefficient and the T2 component, which indicates the degree of diffusion of water molecules in the tissue. If the b value is 0s / mm<sup>2</sup>, the T2 weighted image is displayed, and you can increase the B value to reduce the T2 effect or suppress the water signal<sup>[15]</sup>.

In this study, the diffusion gradient magnetic field was applied in the selection direction of the section, the frequency



coding direction, and the phase coding direction. T2\*-DW-EPI technique with b-value ( $s/mm^2$ ) of 1,000 and the resonant frequency is applied by setting the null point as the inversion time when the water molecule signal reaches the x, y plane. A FLAIR-DW-EPI technique was used to obtain the results of the spread and signal intensity of choroid plexus. Most of choroid plexus did not show high signal intensity in T2\*-DW-EPI test, but showed the same or low signal intensity as the brain parenchyma. The subjects of this study were tested with subjects with high signal strength. As a result of comparing the signal and diffusion degree of choroid plexus between the two techniques, the T2\*-DW-EPI technique showed high signal strength. On the other hand, the FLAIR-DW-EPI technique, which suppressed the water signal, showed the same or low signal intensity as that of the brain parenchyma and was compared. However, there was no difference in the overt diffusion coefficient. Choroid plexus is considered to exhibit high signal strength as the T2 effect remains in the T2\*-DW-EPI technique. Due to the structure of the choroid plexus, the process of generating cerebrospinal fluid in countless capillaries was partially transformed into a sponge-type cystic structure, and it is believed that the diffusion of water molecules was slower than that of stagnant or normal people, resulting in high signal intensity<sup>[16]</sup>. In the results of the FLAIR-DW-EPI test, which suppressed the water signal, the sponge-type cystic structure showed a signal similar to or lower than that of the brain parenchyma as the water signal was suppressed. On the other hand, in the case of acute cerebral infarction and acute cerebral hemorrhage, both techniques showed high signal intensity.

### V. Conclusion

In this study, the signal intensity of the choroid plexus generating cerebrospinal fluid was analyzed by acquiring signals using the T2\*-DW-EPI technique and the FLAIR-DW-EPI technique. Acute cerebral infarction and acute cerebral hemorrhage on diffuse-weighted images were observed with higher signal intensity compared to normal brain in diffuse

images, and the overt diffusivity (ADC) was observed to be low, confirming that it is an excellent technique for diagnosing acute cerebral infarction. In the T2\*-DW-EPI diffusion-weighted image, the FLAIR-DW-EPI technique, which suppressed the water signal, was additionally examined for subjects with high choroid plexus signals and compared and analyzed the signal intensity. As a result, it was confirmed that the FLAIR-DW-EPI technique showed a signal intensity equal to or lower than that of the brain parenchyma, and there was a difference in signal intensity between the two techniques. The results of this study are that in patients with high choroid plexus signals on T2\*-DW-EPI diffusion-weighted images, the FLAIR-DW-EPI technique was additionally examined. It is thought to be useful for the discrimination of cystic structures.

### [Reference]

- [1] Mukherji, Suresh K, Chenevert, Thomas L, Castillo, Mauricio, "*Diffusion-Weighted Magnetic Resonance Imaging*", Journal of Neuro-Ophthalmology, Vol. 22, Issue 2, PP. 118~122(2002)
- [2] Pamela W. Schaefer, P. Ellen Grant, R. Gilberto Gonzalez, "*Diffusion-weighted MR Imaging of the Brain*", Radiology, RSNA 2000 ; 217:331~345(2000)
- [3] Yong Sang, Jingfeng Xu, "*Evaluation of Motor Neuron Injury in ALS by Different Parameters of Diffusion Tensor Imaging*", IEEE Access, Vol. 8, pp. 72381~72394(2020)
- [4] Bhupesh Sharma, Kanishk Luhach, G. T. Kulkarni, "*4-In vitro and in vivo models of BBB to evaluate brain targeting drug delivery*", Brain Targeted Drug Delivery System, pp. 53~101(2019)

- [5] Maarten G. Lansberg, Vincent N. Thijs, Michael W. O'Brien, Juan O. Ali, et al., "*Evolution of Apparent Diffusion Coefficient, Diffusion-weighted, and T2-weighted Signal Intensity of Acute Stroke*", AJNR, Vol. 22, No. 4, pp. 637~633(2001)
- [6] Matthew J. Tait, Samira Saadoun, B. Anthony Bell, Marios C. Papadopoulos, "*Water movements in the brain: role of aquaporins*", Trends in Neurosciences, Vol. 31, Issue 1, pp. 37~43(2008)
- [7] David John Werring, "*Mechanisms of central nervous system damage and recovery in demyelinating and other neurological disorders: structural and functional MRI studies*", Doctoral dissertation, University College London, ProQuest LLC(2016)
- [8] Gary D. Fullerton, "*Magnetic Resonance Imaging Signal Concept*", RadioGraphics, Vol. 7, No. 3, PP. 579~596(1987)
- [9] McRobbie, D., Moore, E., Graves, M., & Prince, M. (2017). "*Getting in Tune: Resonance and Relaxation. In MRI from Picture to Proton*"(pp. 124-143). Cambridge: Cambridge University Press. doi:10.1017/9781107706958.010
- [10] <https://mrimaster.com/characterise%20physics.html> (04-22-2020)
- [11] R. Kates, D. Atkinson, M. Brant-Zawadzki, "*Fluid-attenuated inversion recovery (FLAIR): clinical prospectus of current and future applications*", Top Magn Reson Imaging, Vol. 8, No. 6, PP. 389~396(1996)
- [12] <http://radiopaedia.org> (04-26-2020), "*Double inversion recovery sequence*", rID : 32070 (04-26-2020)
- [13] Filippo Del Grande, Francesco Santini, Daniel A. Herzka, et al., "*Fat-Suppression Technique for 3-T MR Imaging of the Musculoskeletal System*", Radiographics, Vol. 34, No. 1, pp. 217~233(2014)
- [14] [http://www.researchgate.net/figure/Comparison-of-conventional-and-Synthetic-Contrast-MRI-T2-weighted-FLAIR\\_fig6\\_308038621](http://www.researchgate.net/figure/Comparison-of-conventional-and-Synthetic-Contrast-MRI-T2-weighted-FLAIR_fig6_308038621) (04-08-2020)
- [15] Dmitriy A. Yablonskiy, Alexander L. Sukstanskii, "*Theoretical models of the diffusion weighted MR signal*", Published online in Wiley Online Library: 3 June 2010, pp. 661~681(2010), DOI:10.1002/nbm.1520
- [16] Melody P. Lun, Edwin S. Monuki, Maria K. Lehtinen, "*Development and functions of the choroid plexus-cerebrospinal fluid system*", Nat Rev Neurosci, Vol. 16, No. 8, pp. 445~457(2015)

# Determining the Degree of Malignancy on Digital Mammograms by Artificial Intelligence Deep Learning

<sup>1\*</sup>Sang-Bock Lee, <sup>2</sup>Hwunjae Lee, <sup>3</sup>V. R. Singh

Received : 25 June 2020 / Accepted : 15 October 2020 / Published online 28 December 2020

©The Author(s) 2020

**Abstract** In this paper, we propose a method for determining degree of malignancy on digital mammograms using artificial intelligence deep learning. Digital mammography is a technique that uses a low-energy X-ray of approximately 30 KVp to examine the breast. The goal of digital mammography is to detect breast cancer in an early stage by identifying characteristic lesions such as microcalcifications, masses, and architectural distortions. Frequently, microcalcifications appear in clusters that increase ease of detection. In general, larger, round, and oval-shaped calcifications with uniform size have a higher probability of being benign; smaller, irregular, polymorphic, and branching calcifications with heterogeneous size and morphology have a higher probability of being malignant. The experimental images for this study were selected by searching for "mammogram" in the NIH database. The images were converted into JPEG format of 256 X 256 pixels and saved. The stored images were segmented, and edge detection was performed. Most of the lesion area was low frequency, but the edge area was high frequency. DCT was performed to extract the features of the two parts. Similarity was determined based on DCT values entered into the neural network. These were the findings of the study:

- 1) There were 6 types of images representing malignant tumors.
- 2) There were 2 types of images showing benign tumors.
- 3) There were two types of images demonstrating tumors that could worsen into malignancy.

Medical images like those used in this study are interpreted by a radiologist in consideration of pathological factors. Since discrimination of medical images by AI is limited to image information, interpretation by a radiologist is necessary. To improve the discrimination ability of medical images by AI, extracting accurate features of these images is necessary, as is inputting clinical information and accurately setting targets. Study of learning algorithms for neural networks should be continued. We believe that this study concerning recognition of cancer on digital breast images by AI deep learning will be useful to the radiomics (radiology and genomics) research field.

**Keywords:** Breast cancer, Morphology, Feature extraction, Neural networks

---

<sup>1\*</sup>Sang-Bock Lee (✉) **corresponding author**  
(62271)Department of Radiology, Nambu University,  
Nambudae-ro, Gwangsan-gu, Gwangju, Korea

<sup>2</sup>Hwunjae Lee

<sup>1</sup>Department of Radiology, College of Medicine, Yonsei University, 50-1, Yonsei-ro, Seodaemun-gu, Seoul,

<sup>3</sup>V. R. Singh

Director, PDM University, India  
e-mail: vr-singh@ieee.org

## I. Introduction

Research on the principles of radiation discovery and generation in various spectra laid the foundation for modern physics, leading to quantum physics and the theory of relativity<sup>[2]</sup>.



In the late 20th century, radiology was combined with computer technology to develop advanced imaging equipment such as CT, MRI, and PET. These imaging techniques are used to evaluate the anatomy and physiological characteristics of the human body<sup>[3]</sup>. The 4th Industrial Revolution was introduced at the 2016 World Economic Forum and is explained by a variety of new technologies that integrate the physical, biological, and digital worlds based on “big” data and affect all sectors such as economics and industry<sup>[4]</sup>. With the 4th Industrial Revolution, the medical environment is changing from patient diagnosis and treatment to personalized precision medicine, and the center of change is artificial intelligence (AI) technology<sup>[5]</sup>. AI technology aims to be used in the entire process of 'before, during, and after' patient examination using diagnostic imaging equipment, and this will be the basis for precise medical imaging. Breast cancer is the world's leading cancer and cause of death among women. Methods of examining breast cancer include digital breast imaging, MRI, and ultrasound. All the information from these methods are stored and managed as “big” data on a computer<sup>[6]</sup>.

In this paper, we propose a method to recognize cancer in digital breast images through in-depth artificial intelligence. The proposed method will contribute to development of personalized precision medicine.

## II. Materials and Methods

### 1. Digital mammogram

Advances in computer technology and development of new digital imaging detectors have enabled digital mammography, which uses low-energy X-ray of approximately 30 KVp to examine the breast. The goal of digital mammography is to detect breast

cancer at an early stage by identifying characteristic masses or micro-calcifications<sup>[7]</sup>. Like all X-ray images, mammograms are imaged using ionizing radiation, and MO generally uses lower energy X-rays than those for bones (K shell X-ray energy of 17.5 and 19.6 keV) and Rh (20.2 and 22.7 keV)<sup>[8]</sup>. The image is analyzed for detection of abnormalities. Ultrasound, ductogram, PET, and MRI-based breast imaging play a secondary role. Ultrasound is commonly used for new evaluations of masses found during mammography or palpation of masses not visible on X-ray mammograms. MRI evaluates suspected disease and is useful in enabling surgical method changes such as those associated with breast-conserving mastectomy in preoperative evaluation of patients with confirmed breast cancer<sup>[9]</sup>. Recently, the tomosynthesis technique has been used as a digital mammography method<sup>[10]</sup>.

### 2. Breast cancer basic morphology

Breast cancer has some characteristic lesions such as microcalcifications, masses, and architectural distortions. Breast asymmetry can also be a breast cancer indicator. Microcalcifications are small-sized lesions, typically in the range of 0.05 to 1 mm, and relatively difficult to detect. Microcalcifications are bright on imaging and have various sizes, shapes, and distributions. In some cases, these lesions have low contrast due to a reduced intensity difference between suspicious areas and the surroundings. Another reason for difficult detection of these lesions is the proximity to the surrounding tissues. In dense tissues, suspicious areas are nearly invisible as a result of tissue superimposition. Some anatomic structures such as fibrous strands, breast borders, or hypertrophied lobules are similar to microcalcifications on mammographic imaging<sup>[11]</sup>. Frequently, microcalcifications appear in clusters, resulting in easier detection<sup>[12]</sup>. There is a high

correlation between presence of microcalcifications and breast cancer, particularly when the microcalcifications are clustered. Therefore, accurate detection of microcalcifications is essential to early detection of the majority of breast cancers<sup>[13]</sup>. In general, larger, round, and oval-shaped calcifications with uniform size have a higher probability of being benign; smaller, irregular, polymorphic, and branching calcifications with heterogeneous size and morphology have a higher probability of being malignant<sup>[14]</sup>. Masses appear as dense regions of

different sizes and properties and can be circular, oval, lobular, or irregular and spiculated. Mammographic masses can be described as follows:

- circumscribed, which are well-defined with distinctly demarcated borders;
- obscured, which are hidden by superimposed or adjacent tissue;
- micro-lobulated, which have undulating circular borders;
- ill-defined, which have poorly defined scattered borders;
- spiculated/stellate, which are radiating thin lines.

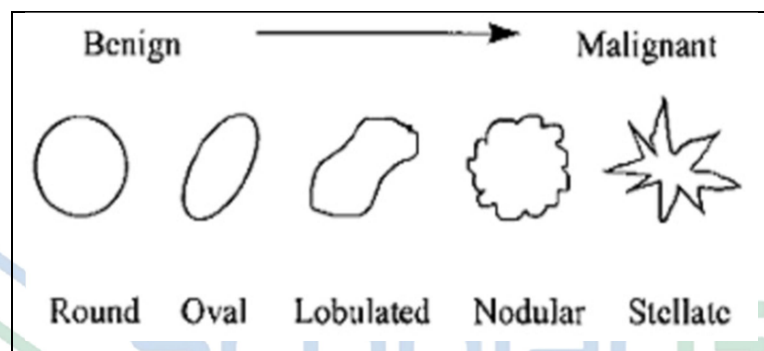


Figure 1. Morphologic spectrum of mammographic masses<sup>[15]</sup>

### 3. Image segmentation and edge detection

In digital image processing, image segmentation is the process of dividing a digital image into multiple segments to simplify the representation of the image and convert it to more meaningful and easier to analyze data. More precisely, image segmentation is the process of assigning labels to all pixels in an image so that pixels with the same label share certain characteristics<sup>[16]</sup>. The result of image segmentation is a set of segments that represents the entire image or a set of outlines extracted from the image. All pixels in a segment are similar in some way such as color, intensity, or texture. Adjacent areas differ significantly with respect to the chosen characteristics. Image segmentation is commonly used to find objects and boundaries in an image. The

simplest image segmentation method is called the threshold method<sup>[17]</sup>. This method converts a grayscale image to a binary image based on threshold, the choice of which is key to detection<sup>[17]</sup>. Several popular methods are used in industry, including the maximum entropy method, balanced histogram threshold, Otsu method, and k-means clustering<sup>[17]</sup>. Edge detection involves a variety of mathematical methods that aim to identify points in a digital image in which image brightness is discontinuous. The point at which the image brightness changes rapidly consists of curved segments, commonly called edges<sup>[18]</sup>. Identification of a discontinuity in a one-dimensional signal is called step detection, and identification of signal discontinuity over time is called change detection<sup>[19]</sup>. Edge detection is the primary tool in image processing, especially feature

detection and feature extraction. Edge thinning is a technique used to remove unwanted spurious points on the edges of an image. This technique is used after filtering the “noise” from the image, detecting the edges using the edge operator, and smoothing the edges to an appropriate threshold<sup>[19]</sup>. This process creates an edge element that is 1 pixel thick by removing all unwanted points and applying them

carefully.

The advantages of edge detection are:

1. Sharp and thin edges increase the efficiency of object recognition.
2. Use of Hough transformation to detect lines and ellipses results in high-quality thinning.
3. When an edge is a boundary of a segment and becomes thinner, image parameters are easily obtainable without the need for algebra<sup>[20]</sup>.

Table 1. Segmentation and edge detection function

```
% Segmentation and edge detection function
I = imread('Exam-image');
subplot(1,3,1);imshow(I); title('Original Image');
[~,threshold] = edge(I,'sobel'); fudgeFactor = 0.5;
BWs = (I >= 127); % threshold 127
se90 = strel('line',3,90); se0 = strel('line',3,0);
BWsdil = imdilate(BWs,[se90 se0]);
BWdfill = imfill(BWsdil,'holes');
BWnobord = imclearborder(BWdfill,4);
seD = strel('diamond',1);
BWfinal = imerode(BWnobord,seD);
BWfinal = imerode(BWfinal,seD);
subplot(1,3,2); imshow(BWfinal);
title('Segmented Image');
subplot(1,3,3); imshow(edge(BWfinal));
title('Edge detection');
```

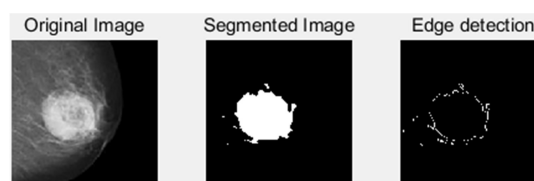


Figure 2. Segmentation and edge detection of an image

#### 4. Feature extraction by DCT

Feature extraction by DCT is an orthogonal transformation coding method using a discrete cosine function as a coefficient for transforming an image

signal on a time axis onto a frequency axis. In 1988, ITU-T was adopted as the video compression technology of the H.261 encoding method for conference calls. ITU-T was subsequently adopted

by MPEG, the international standard for video compression, and is now the mainstream of high-efficiency encoding and compression of video<sup>[21]</sup>. Discrete cosine transformation (DCT) decomposes the image signal on the time axis and transforms it into a small, low-frequency domain with multiple signal powers. Since the power of the image signal is concentrated in the low-frequency region, quantizing with proper allocation produces the entire bit<sup>[22]</sup>. The result can be compressed with a small amount of data.

Though optimized transformation includes the Karen-Lube transformation (KLT), for video signals, DCT can achieve high coding efficiency approximating that of the KLT<sup>[23]</sup>. In this study, the DCT was extracted as follows. Since energy is concentrated in the low-frequency region, many kinds of feature parameters of DCT coefficients are extracted there. Table 2 shows the block location of the extraction amplitude characteristic parameters.

Table 2. DCT function

```
% DCT Function
in_img=imread('Exam_Image');
fileout=fopen('Out-File','w');
imshow(in_img);
dct_img=rgb2gray(in_img); dct_img=dct2(dct_img);
figure; imshow(log(abs(dct_img)));
disp('starting extraction step for summations of each blocks.....');
disp('...'); sum=zeros(8,8);
for h=0:7
    for v=0:7
        hap=0;
        for hp=1:16
            for vp=1:16
                hap=hap+abs(dct_img(h*16 + hp , v*16 + vp));
            end
        end
        sum(v+1, h+1)=hap;
    end
end
disp('normalization about summaiton of each blocks');
disp('...'); sumline=zeros(1,32);
line=0;
for m=3:8
    k=0;
    for n=1:10
        m=m-1;
        k=k+1;
        if m==0 break
        end
        line=line+1;
        sumline(1,line)=sum(m,k);
    end
    if n==32 break
    end
end
Max = -10000;
Min = 10000;
for su=(1:32)
    if ( sumline(su) > Max )
        Max = sumline(su);
    end;
    if ( sumline(su) < Min )
        Min = sumline(su);
    end;
end;
```

```

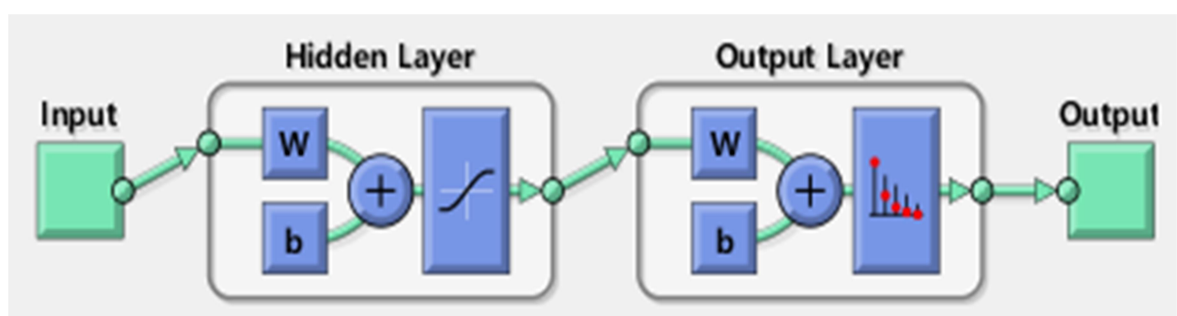
for su=(1:32)
    sumline(su) = ((sumline(su)- Min) / (Max -Min)) - 0.5;
end;
disp('saving normaliziton data for summation of each blocks');
disp('...'); for su=(1:32)
    fprintf(fileout,'%10.4f',sumline(su));
end;
fclose(fileout);

```

## 5. Neural network

Artificial intelligence (AI) is generally limited to a specific task. For example, most AI technologies are applied to a specific task such as automatic language translation, image recognition, speech recognition, and development and analysis of artificial neural network structures can be said to be artificial intelligence in a narrow sense<sup>[24]</sup>. Artificial intelligence is being applied to various fields with development and power of technology related to the 4<sup>th</sup> Industrial Revolution. In particular, use of AI in the medical field has spread rapidly. To date, representative uses of AI in the medical field are related to medical services in various fields ranging from secondary analysis of medical data to predicting and diagnosing diseases and analysis of medical

images<sup>[25]</sup>. In general, AI-based medical devices contain software that can improve performance by analyzing medical data and medical devices including the same. Artificial intelligence-based medical systems can be viewed as competitive with healthcare professionals, but use of AI in the medical field should be complementary to, rather than competitive with, the work of medical personnel<sup>[25]</sup>. Use of AI-based medical systems is rapidly expanding, particularly in the 4 areas of robotic surgical systems, virtual nursing systems, medical diagnostic systems, and medical imaging systems<sup>[26]</sup>. In particular, AI-based medical imaging analysis performs the most important functions in medical diagnosis and, along with pathology-related data, is a key area of AI-based medical technology<sup>[26]</sup>.



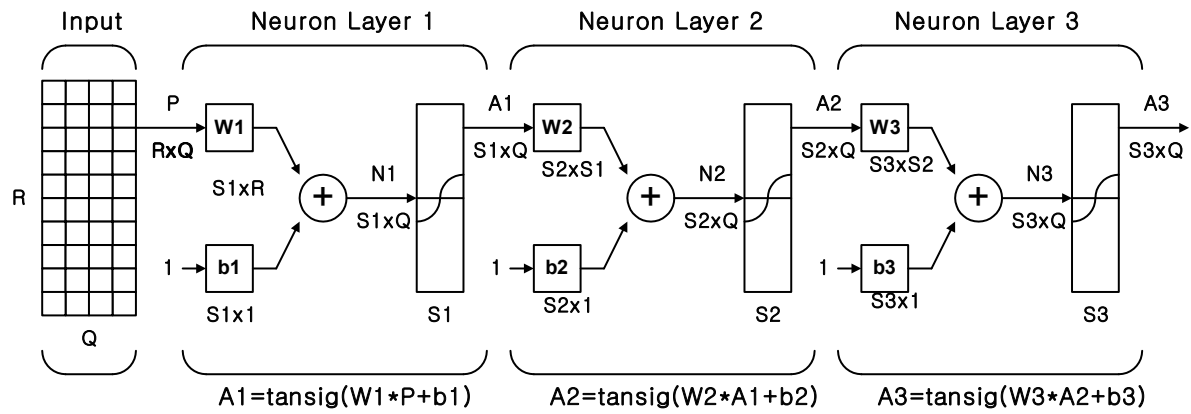


Figure 3. Neural network diagram

### III. Experiment

The experimental images for this study were selected by searching for "mammogram" in the NIH database. The images selected for the experiment were converted into a JPEG format of 256 X 256

pixels and saved. The stored experimental images were segmented, and edge detection was performed. Most of the segments are low frequency, but the edges are of high frequency. DCT was performed to extract the features of the two parts, and similarity was determined based on DCT values input into the neural network. Figure 4 shows the experimental procedure.

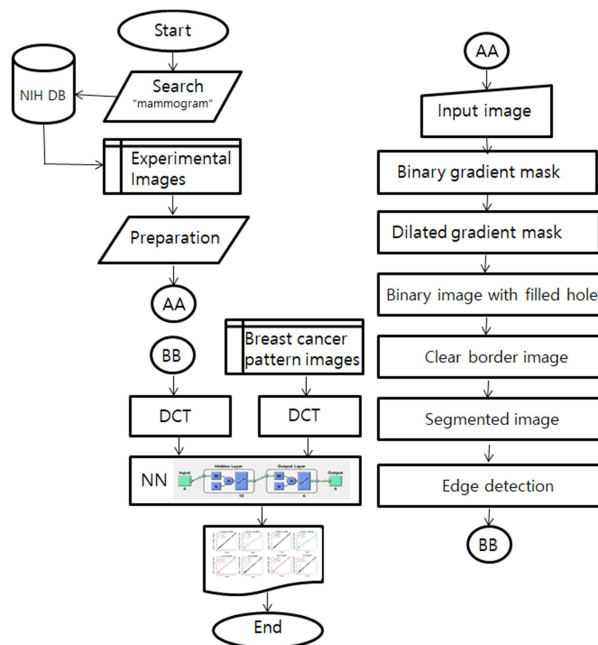
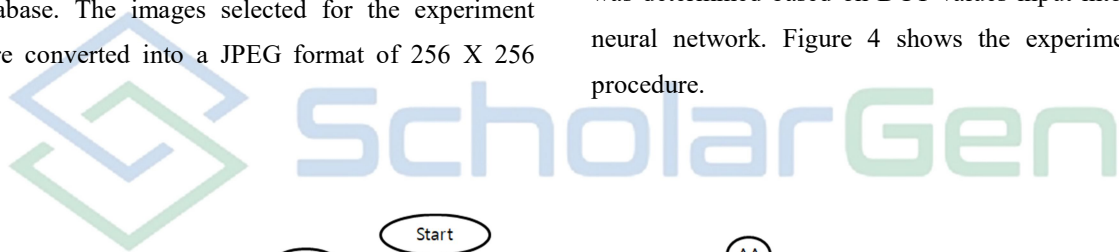


Figure 4. Flowchart of the experimental procedure

### 1. Image segmentation and edge detection

In the breast images for the experiment, the cancer area was segmented using the basic morphology, and the edge was detected. Segmentation is based on the large difference in contrast of a cancer area compared to the surroundings. Contrast change was detected by calculating the image slope. To create a binary mask including the segmented region, a gradient image was calculated, and a threshold value of 127 or more was applied. The edge was detected using Matlab's function `edge()` and `sobel()` operators. Next, the image was expanded. In the binary gradient mask, a line representing the high contrast of the image is displayed. Difficulty arises in recognizing the outline of the desired object with these lines. Compared

with the original image, there is a gap between the lines surrounding the object of the tilt mask. This line spacing disappears when the image is expanded by the `sobel()` operation using a linear structure element. Two orthogonal linear structural elements were created using the `strel()` function. The next step was filling the inner gap. The expanded gradient mask has a well-arranged cell outline, but holes exist inside the cell. To fill these holes, the `imfill()` function was used. The next step was to remove the objects in contact with the border. All objects in contact with the border of the image were removed using the `imclearborder()` function. To remove the diagonal connection, the connectivity of the `imclearborder()` function was set to 4. Finally, the image was eroded twice with a diamond structure element, created using the `strel()` function, for smoothing.

Table 3. Edge detection of breast cancer basic morphology











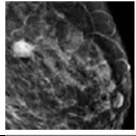
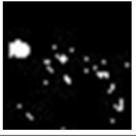

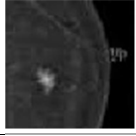
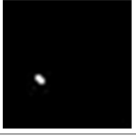

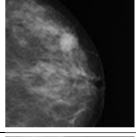

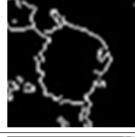
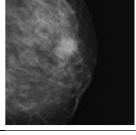


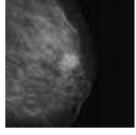


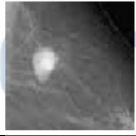


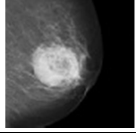

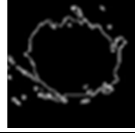
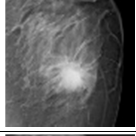


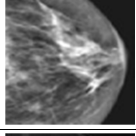


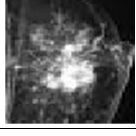


Type	Basic morphology	Edge detection
Round		
Oval		
Lobulated		
Nodular		
Stellate		



Table 4. Segmentation and edge detection of experimental images

	Image	Segment	Edge
Img_1			
Img_2			
Img_3			
Img_4			
Img_5			
Img_6			
Img_7			
Img_8			
Img_9			
Img_10			

**2. Perform DCT**

The features of the experimental images and

breast cancer basic morphological images were extracted from the edge detection image using Matlab's dct() function.



Table 5. Extracted-feature values of basic morphological images of breast cancer

Round	0.363	0.5	0.039	0.01	0.024	-0.02	0.082	0.056	-0.049	-0.12	0.074	0.21	-0.184	-0.1	-0.15	0.006	-0.07	-0.17	-0.15	0.166	-0.19	-0.17	-0.12	-0.18	-0.2	0.072	-0.5	-0.5	-0.5	-0.5	
Oval	0.5	0.227	-0.17	0.08	-0.174	-0.16	-0.18	-0.24	-0.31	-0.1	-0.06	-0.2	-0.25	-0.275	-0.2	-0.03	-0.1	-0.19	-0.26	-0.23	-0.19	-0.19	-0.07	-0.01	-0.26	-0.28	-0.18	-0.5	-0.5	-0.5	-0.5
Lobulated	0.5	0.492	-0.05	0.07	-0.044	0.015	0.052	0.203	-0.047	-0.19	0.022	0.22	-0.03	-0.115	-0.1	-0.15	-0.04	-0.06	-0.2	-0.17	-0.06	-0.22	-0.24	-0.2	-0.25	-0.21	-0.21	-0.5	-0.5	-0.5	-0.5
Nodular	0.5	0.444	0.252	0.07	0.161	0.111	0.053	0.005	0.135	0.179	0.002	-0	-0.02	0.053	0.15	-0.03	-0.08	-0.03	-0.13	0.219	0.229	-0.07	-0.08	-0	-0.03	-0.05	0.24	-0.5	-0.5	-0.5	-0.5
stellate	0.5	0.374	-0.04	0.04	-0.082	0.007	-0.13	-0.1	-0.057	-0.14	-0.08	-0.1	-0.11	-0.099	-0.1	-0.16	-0.14	-0.21	-0.19	-0.12	3E-04	-0.15	-0.17	-0.24	-0.19	-0.13	-0.12	-0.5	-0.5	-0.5	-0.5

Table 6. Extracted-feature values of experimental images

img_1	0.4	0.5	0.313	0.195	0.2216	0.1699	0.0646	0.188	0.116	-0.012	-0.017	-0.025	-0.061	-0.0344	-0.104	-0.1507	-0.092	-0.096	-0.169	-0.127	-0.286	-0.219	-0.2	-0.146	-0.195	-0.1824	-0.24	-0.5	-0.5	-0.5	-0.5
img_2	0.295	0.4237	0.369	0.161	0.1678	0.5	0.082	-0.024	0.203	0.133	0.0636	-0.058	-0.017	-0.0236	0.1134	0.0715	-0.031	-0.137	-0.078	-0.079	-0.064	-0.084	-0.08	-0.181	-0.188	-0.1018	-0.22	-0.5	-0.5	-0.5	-0.5
img_3	0.37	0.5	0.177	0.326	0.2006	0.1807	0.3051	0.156	0.159	0.0019	0.1257	0.0248	0.0127	-0.015	-0.174	-0.041	0.0159	-0.05	-0.096	-0.092	-0.286	-0.117	-0.12	-0.093	-0.097	-0.1648	-0.24	-0.5	-0.5	-0.5	-0.5
img_4	0.5	0.3899	0.234	0.28	0.0284	0.049	0.0617	0.054	-0.1	-0.168	-0.08	-0.076	-0.076	-0.2008	-0.329	-0.2391	-0.18	-0.182	-0.22	-0.302	-0.348	-0.4	-0.33	-0.266	-0.303	-0.3406	-0.43	-0.5	-0.5	-0.5	-0.5
img_5	0.5	0.4383	0.345	0.447	0.348	0.1193	0.2834	0.402	0.173	-0.078	0.1241	0.1311	0.095	-0.0817	-0.274	-0.0811	-0.099	-0.02	-0.029	-0.248	-0.385	-0.304	-0.14	-0.079	-0.135	-0.2804	-0.36	-0.5	-0.5	-0.5	-0.5
img_6	0.343	0.5	0.399	0.291	0.4593	0.2666	0.1895	0.188	0.311	0.0303	0.1298	0.3581	0.1709	0.254	0.027	0.0425	0.1899	0.2976	0.1251	0.233	-0.063	-0.056	0.024	0.1082	0.1463	0.0408	0.146	-0.5	-0.5	-0.5	-0.5
img_7	0.366	0.5	0.18	0.396	0.2299	0.0622	0.1309	0.19	0.054	0.0131	0.0013	0.075	-0.056	-0.0031	-0.038	-0.11	-0.013	-0.012	-0.071	-0.047	-0.118	-0.131	-0.08	-0.062	-0.086	-0.1098	-0.08	-0.5	-0.5	-0.5	-0.5
img_8	0.378	0.5	0.18	0.344	0.1778	0.0571	0.2143	0.309	0.078	0.0381	0.1736	0.2377	0.0654	-0.0424	-0.065	0.0495	0.1468	0.1256	0.0127	-3E-04	-0.036	-0.021	0.129	0.0666	0.0043	0.0218	-0.06	-0.5	-0.5	-0.5	-0.5
img_9	0.41	0.5	0.222	0.348	0.1995	0.1416	0.2325	0.251	0.191	0.0503	0.1228	0.2107	0.1475	0.1472	-0.077	0.0229	0.1317	0.0759	0.1361	0.0646	-0.052	-0.103	-0.03	-0.012	0.014	0.0743	0.039	-0.5	-0.5	-0.5	-0.5
img_10	0.423	0.5	0.097	0.321	0.3954	0.0838	0.0984	0.191	0.262	0.3112	0.0093	0.022	0.1533	0.1659	0.0838	0.0116	0.0237	0.0037	0.1661	0.4413	0.0849	0.0204	-0.06	-0.043	0.0116	0.1062	0.304	-0.5	-0.5	-0.5	-0.5

### 3. Perform similarity determination

Experimental image data of *Img\_1* to *Img\_10* were input into the neural network to determine which type of breast cancer basic morphology was similar to the experimental image. Neural networks were trained by inputting breast cancer basic morphology data of “Round, Oval, Lobulated, Nodular, and Stellate” into each set

of experimental image data.

Input examination image ‘*Img\_1*’ is a 1 x 32 matrix, representing static data of 32 samples of 1 element. Target breast cancer basic morphology ‘Round’ is a 1 x 32 matrix, representing static data of 32 samples 1 element. The experiment was conducted as below. Figures 5 to 8 show performance, training state, error histogram, and fit of the method.

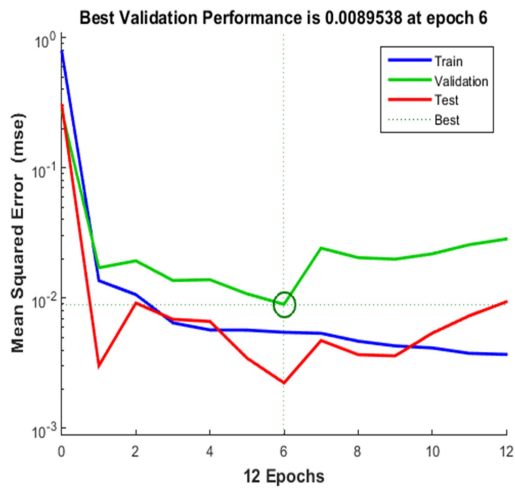


Figure 5. Performance

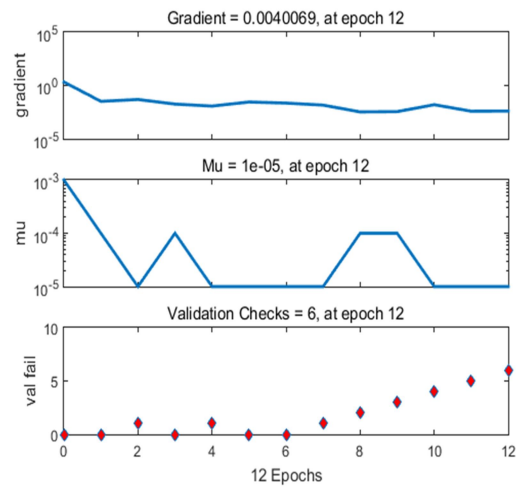


Figure 6. Training state



Figure 7. Error histogram

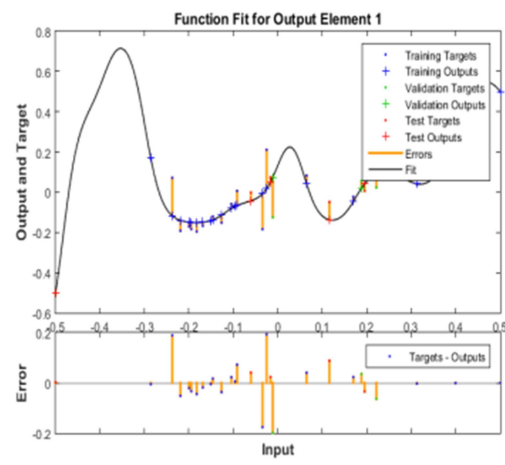


Figure 8. Fit

Figure 9 shows regression graphs of experimental image data when 'Img\_1' was the neural network input and breast cancer basic

morphology 'Round' was the neural network target. The figure shows the degree of regression in R-value.

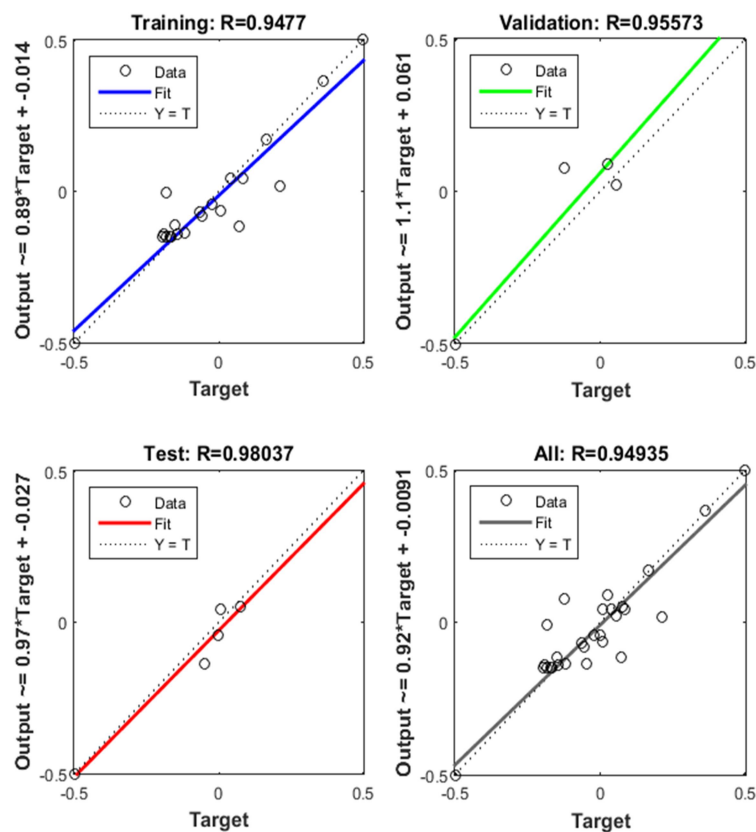


Figure 9. Regression

#### IV. Results and discussion

To determine the degree of malignancy in breast imaging, the similarity to the previously studied breast cancer basic morphology was examined. The results are shown in Table 7.

1. Img\_1 showed the highest R value of 0.9874, which indicates similarity to Stellate.
2. Img\_2 showed the highest R value of 0.9246, indicating similarity to Nodular.
3. Img\_3 showed the highest R value of 0.978183, which indicates similarity to Stellate.
4. Img\_4 showed the highest R value of 0.96967, indicating similarity to Stellate.
5. Img\_4 showed the highest R value of 0.94653,

indicating similarity to Stellate.

6. Img\_4 showed the highest R value of 0.92613, indicating similarity to Round.

7. Img\_4 showed the highest R value of 0.90947, indicating similarity to Nodular.












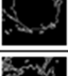

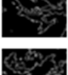

8. Img\_4 showed the highest R value of 0.97085, indicating similarity to Stellate.

9. Img\_4 showed the highest R value of 0.9343, indicating similarity to Round.

10. Img\_4 showed the highest R value of 0.97475, indicating similarity to Stellate.

Images similar to malignant cancer were Img\_1, Img\_3, Img\_4, Img\_5, Img\_8, and Img\_10. The images similar to the nodular shape were Img\_2 and Img\_7. The image similar to benign was Img\_6.

Table 7. Results of examination

Basic morphology Exam_img		Benign----->malignant				
		Round	Oval	Lobulated	Nodular	Stellate
Image	edge					
Img_1		0.87409	0.90754	0.88755	0.9119	0.9874
Img_2		0.80258	0.028656	0.77009	0.9246	0.90448
Img_3		0.93114	0.86929	0.90165	0.88674	0.978183
Img_4		0.82084	0.90451	0.95427	0.86761	0.96967
Img_5		0.83403	0.93647	0.93425	0.89497	0.94653
Img_6		0.92613	0.35626	0.92289	0.84943	0.85255
Img_7		0.79847	0.75773	0.89233	0.90947	0.85966
Img_8		0.89469	0.85434	0.91494	0.92007	0.97035
Img_9		0.9343	0.93303	0.84103	0.85129	0.91545
Img_10		0.87204	0.68936	0.82704	0.94892	0.97475

### V. Conclusion

In this paper, a method to determine breast cancer basic morphology associated with image shapes is presented. For similarity discrimination, the experimental breast cancer image was segmented based on the cancer region, and the edge of the segmented cancer region was detected. Features were extracted from the detected edge image of the experimental image by DCT. The breast cancer basic morphology image was also edge detected, and features were extracted by DCT. AI learning for similarity determination consisted of the input layer, hidden layer, and output layer; and iterative learning occurred through the error backpropagation method. The neural network was trained by sequentially

inputting the feature values of the experimental image and the target data of the neural network as the breast cancer basic morphology images (Round, Oval, Lobulated, Nodular, and Stellate).

The neural network training results of 10 experimental images are as follows.

- 1) There were 6 images representing malignant tumors.
- 2) There were 2 images showing benign tumors.
- 3) There were two images that could worsen into malignant tumors.

The experimental images selected for the experiment were from the breast cancer image database. Medical images are interpreted by a

radiologist in consideration of pathological factors other than imaging. Since the discrimination of medical images by AI to date is limited to image information, a radiologist's input is necessary. To improve the discrimination ability of medical images by AI, extracting accurate features of medical images and inputting clinical information are necessary in addition to accurately setting targets. The study of learning algorithms for neural networking should be continued. We believe that this study concerning recognition of cancer on digital breast images by AI deep learning will be useful to the radiomics (radiology and genomics) research field.

### Competing interests

The authors declare that there is no conflict of interest regarding the publication of this paper

### [Acknowledgment]

This study was supported by a National Research Foundation of Korea (NRF) grant funded by the Korean government (MEST) (NRF-2020R1I1A1A01060851), and in part by research funds from Nambu University, 2020.

### [References]

- [1] Simone Natale, "**THE INVISIBLE MADE VISIBLE**", Journal of Media History, Volume 17, Issue 4, pp. 345~358(2011).
- [2] Stephen T. Thornton, Andrew Rex, "**Modern Physics for Scientists and Engineers**", Publisher, Physics and Astronomy: Charles Hartford, PP. 272~298(2013)
- [3] Bruce H. Hasegawa, Koji Iwata et al, "**Dual-Modality Imaging of Function and Physiology**", Academic Radiology, Volume 9, Issue 11, pp. 1305~1321(2002)
- [4] Klaus Schwab, "**The Fourth Industrial Revolution**", Crown Business, pp. 6~21(2016)
- [5] Chayakrit Krittanawong, HongJu Zhang, et al, "**Artificial Intelligence in Precision Cardiovascular Medicine**", JACC, Volume 69, Issue 21, pp. 2655~2664(2017)
- [6] Christiane Katharina Kuhl, Rita K. Schmutzler, et al, "**Breast MR Imaging Screening in 192 Women Proved or Suspected to Be Carriers of a Breast Cancer Susceptibility Gene: Preliminary Results**", Radiology, Vol. 215, No. 1, pp. 267~279 (2000)
- [7] Clarisse Dromain & Fabienne Thibault et al, "**Dual-energy contrast-enhanced digital mammography: initial clinical results**", Eur Radiol., Volume 21, pp. 565~574(2011)
- [8] Azhar Taha Adam Mohamed, "**Evaluation of Radiation Dose to Patients During Mammography Examination**", Sudan Academy of Science(SAS) Atomic Energy Console(2018)
- [9] Virginia Gonzalez, Kerstin Sandelin, et al, "**Preoperative MRI of the Breast (POMB) Influences Primary Treatment in Breast Cancer: A Prospective, Randomized, Multicenter Study**", World Journal of Surgery, Volume 38, pp. 1685~1693(2014)
- [10] Mark A. Helvie, "**Digital Mammography Imaging: Breast Tomosynthesis and Advanced Applications**", Radiol Clin North Am., Vol. 48, No. 5, pp. 917~929(2010)
- [11] Deepa Sankar, Tessamma Thomas, "**Fractal Features based on Differential Box Counting**"



**Method for the Categorization of Digital Mammograms**", IJCISIM, Vol.2, pp. 11~19(2010)

[12] Weijie Chen, Maryellen L. Giger, et al. "**Computerized interpretation of breast MRI: Investigation of enhancement variance dynamics**". Med. Phys., Vol. 31, No. 5, pp. 1076~1082(2004)

[13] H. Li, K. J. R. Liu, S-C.B. Lo, "**Fractal Modeling and Segmentation for the Enhancement of Microcalcification in Digital Mammograms**", ISR Technical Research Report, pp 1~33 (2007)

[14] Arnau Oliver, Xavier Llad'o, et al. "**False Positive Reduction in Mammographic Mass Detection Using Local Binary Patterns**", MICCAI 2007: Medical Image Computing and Computer-Assisted Intervention – MICCAI, pp. 286-293(2007)

[15] L.M. Bruce ; R.R. Adhami, "**Classifying mammographic mass shapes using the wavelet transform modulus-maxima method**", IEEE Transactions on Medical Imaging, Volume 18, Issue 12, pp. 1170~1177(1999)

[16] Dzung L, Phamy, Chenyang Xu , Jerry L. Prince, "**Current Methods in Medical Image Segmentation**", Annual Review of Biomedical Engineering, Volume 2, pp. 315~337(2000)

[17] K. Bhargavi, "**A Survey on Threshold Based Segmentation Technique in Image Processing**", IJIRD, Vol. 3, Issue 12, pp. 234~239(2014)

[18] Ali Can, Hong Shen, J.N. Turner, H.L. Tanenbaum, B. Roysam, "**Rapid automated tracing and feature extraction from retinal fundus images using direct exploratory algorithms**", IEEE Transactions on Information Technology in Biomedicine, Volume 3, Issue 2, pp. 125~138(1999)

[19] Wenshuo Gao, Xiaoguang Zhang, Lei Yang, Huizhong Liu, "**An improved Sobel edge detection**", 2010 3rd International Conference on Computer Science and Information Technology, INSPEC Accession Number: 11520501

[20] Tony Lindeberg, "**Detecting salient blob-like image structures and their scales with a scale-space primal sketch: A method for focus-of-attention**", International Journal of Computer Vision volume 11, pp. 283~318(1993)

[21] Tokumichi Murakami, "**The Development and Standardization of Ultra High Definition Video Technology**", Springer Link Part of the Signals and Communication Technology book series, High-Quality Visual Experience, pp. 81-135(2010)

[22] Bertran Denis, Jean Cote, Rene Laprise, "**Spectral Decomposition of Two-Dimensional Atmospheric Fields on Limited-Area Domains Using the Discrete Cosine Transform (DCT)**", American Meteorological Society, Volume 130, Issue 7, pp. 1812~1829(2002)

[23] Barbara Penna, Tammam Tillo, Enrico Magli, Gabriella Olmo, "**Transform Coding Techniques for Lossy Hyperspectral Data Compression**", IEEE Transactions on Geoscience and Remote Sensing, Volume 45, Issue 5, pp. 1408~1421(2007)

[24] Dennis M. Dimiduk, Elizabeth A. Holm, Stephen R. Niezgod, "**Perspectives on the Impact of Machine Learning, Deep Learning, and Artificial Intelligence on Materials, Processes, and Structures Engineering**", Springer Integrating Materials and Manufacturing Innovation, Volume 7, pp. 157~172(2018)

[25] Geert Litjens, Thijs Kooi, Babak Ehteshami Bejnordi, et al. "*A Survey on Deep Learning in Medical Image Analysis*", *Medical Image Analysis*, Volume 42, pp. 60~88(2017)

[26] Werner Horn, "*AI in medicine on its way from knowledge-intensive to data-intensive systems*", *Artificial Intelligence in Medicine*, Volume 23, Issue 1, pp. 5~12(2001)



# Peak Signal-to-Noise Ratio Evaluation of Server Display Monitors and Client Display Monitors in a Digital Subtraction Angiography Devices

<sup>1,2</sup>Hwunjae Lee, <sup>3\*</sup>Junhaeng Lee

Received: 14 July 2020 / Accepted: 26 October 2020 / Published online: 28 December 2020

©The Author(s) 2020

## Abstract

This study evaluated PSNR of server display monitor and client display monitor of DSA system. The signal is acquired and imaged during the surgery and stored in the PACS server. After that, distortion of the original signal is an important problem in the process of observation on the client monitor. There are many problems such as noise generated during compression and image storage/transmission in PACS, information loss during image storage and transmission, and deterioration in image quality when outputting medical images from a monitor. The equipment used for the experiment in this study was P's DSA. We used two types of monitors in our experiment, one is P's company resolution 1280×1024 pixel monitor, and the other is W's company resolution 1536×2048 pixel monitor.

The PACS Program used MARO-view, and for the experiment, a PSNR measurement program using Visual C++ was implemented and used for the experiment. As a result of the experiment, the PSNR value of the kidney angiography image was 26.958dB, the PSNR value of the lung angiography image was 28.9174 dB, the PSNR value of the heart angiography image was 22.8315dB, and the PSNR value of the neck angiography image was 37.0319 dB, and the knee blood vessels image showed a PSNR value of 43.2052 dB, respectively. In conclusion, it can be seen that there is almost no signal distortion in the process of acquiring, storing, and transmitting images in PACS. However, it suggests that the image signal may be distorted depending on the resolution and performance of each monitor. Therefore, it will be necessary to evaluate the performance of the monitor and to maintain the performance.

**Keyword :** DSA system, Display monitor, Compression, PACS, PSNR

<sup>1,2</sup>Hwunjae Lee

<sup>1</sup>Department of Radiology, College of Medicine, Yonsei University, 50-1, Yonsei-ro, Seodaemun-gu, Seoul, Korea  
<sup>2</sup>YUHS-KRIBB Medical Convergence Research Institute, College of Medicine, Yonsei University, Seoul, Korea

<sup>3\*</sup>Junhaeng Lee (✉) **corresponding author**  
(62271)Department of Radiology, Nambu University 23 Chumdan Jungang-ro, Gwangan-gu, Gwangju, Korea

## I. Introduction

With the development of digital technology, the medical field is also rapidly digitizing. The development of the fourth industry is expected to accelerate the digitalization of the medical industry<sup>[1]</sup>. The vast amount of digital medical images generated in medical institutions are stored in PACS (Picture Archiving and Communication System) servers to become big data. Such big data is the foundation for the development of artificial



intelligence technology<sup>[2]</sup>. When transmitting medical images in PACS, noise may occur on the network. The image is compressed, stored, and transmitted to improve these limitations and to ensure smooth server operation and seamless medical treatment<sup>[3]</sup>. In order to use the compressed medical image for treatment, it must be completely restoration. In the case of compression and restoration, even a small loss of information affects treatment, which increases the rate of false diagnosis<sup>[4]</sup>. A high-resolution image without loss must be output from a reading monitor and a medical monitor, and an image without noise and distortion of the image must be output on a general monitor. In order to improve these problems, an objective and reliable evaluation should be made. However, until now, the quality evaluation part of medical images is limited to display devices<sup>[5]</sup>. Distortion of image signals can occur in signal acquisition and display, compression storage and transmission, restoration and display exaggeration<sup>[6]</sup>. In this paper, by

evaluating the PSNR of the server display monitor and the client display monitor of the DSA system, we propose an evaluation method for noise and image quality deterioration occurring in the process from acquiring the server display signal to the client display monitor.

## II. PSNR evaluation of digital medical images

PSNR is most easily defined via the mean squared error ( $MSE$ )<sup>[7]</sup>. Given a noise-free  $m \times n$  monochrome image  $I$  and its noisy approximation  $K$ ,  $MSE$  is defined as:

$$MSE = \frac{1}{m n} \sum_{i=0}^{m-1} \sum_{j=0}^{n-1} [I(i, j) - K(i, j)]^2$$

The PSNR (in dB) is defined as:

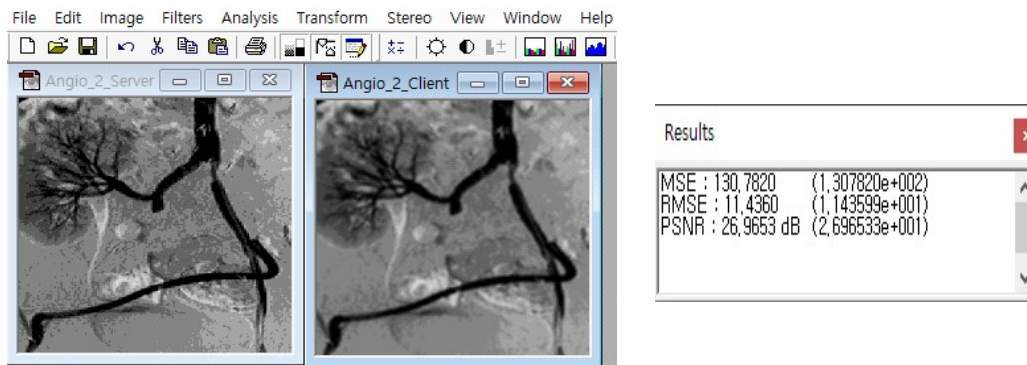
$$\begin{aligned} PSNR &= 10 \cdot \log_{10} \left( \frac{MAX_I^2}{MSE} \right) \\ &= 20 \cdot \log_{10} \left( \frac{MAX_I}{\sqrt{MSE}} \right) \\ &= 20 \cdot \log_{10}(MAX_I) - 10 \cdot \log_{10}(MSE) \end{aligned}$$

Here,  $MAX_I$  is the maximum possible pixel value of the image. When the pixels are represented using 8 bits per sample, this is 255. More generally, when samples are represented using linear PCM with  $B$  bits per sample,  $MAX_I$  is  $2^B - 1$ . If the two images are the same without any difference in quality loss, the MSE is 0 and the PSNR is infinite more than 50dB. In the case of lossless image, the MSE is 0, and the PSNR is not defined. 50dB is regarded as the original image, and if the difference is more than 11dB, it is viewed as a similar image<sup>[8]</sup>. In particular, since medical images are images dealing with human life, serious

misdiagnosis can occur even with small loss of image quality. Therefore, the quality level should be over 30dB<sup>[9]</sup>. The standard deviation tells us how far the observations are from the mean. Currently, image evaluation by PSNR is widely used for image quality evaluation of various images, and occupies a very important weight. Specifically, it is widely used for evaluation of compression codes such as deterioration of image quality and noise generation of compressed images during image compression. Compression is a type of coding, and coding refers to both encoding that changes arbitrary data for a specific purpose and decoding that restores the changed data to its original state.

Lossless compression is also referred to as reversible compression, and when decompressing a compressed image, original information can be restored without loss, and has a lower compression rate than loss compression. Representatively, Huffman Coding is used. Loss compression is also referred to as irreversible compression, and is a compression method that does not match the original data before compression because some data is lost when compressed data is restored again. Image compression generally uses image conversion that removes

redundancy between pixels of an image, reducing the size of the original data and storing it. A loss compression has a high compression rate instead of corrupting information and not recovering it again. Representatively, Cosine Transform Coding is used. A lossless compression method is widely used to prevent loss of information and deterioration of image quality that occur when compressing an image. At this time, PSNR is used to measure the quality between the original image and the compressed image and to evaluate the compression codec.<sup>[10]</sup>



(a) Input of experimental images (b) PSNR experimental result  
Figure 1. Execution of image processing program written in C++

### III. Materials and methods

Digital subtraction angiography (DSA) digitizes the analog electrical signal obtained from a fluorescence multiplier and a camera by an AD converter, and then subtracts the blood vessel image and the mask image in the image processing process to obtain a blood vessel image. In

other words, it is a method in which the density of the image is digitally digitalized to remove the overlapping part, thereby erasing bone and soft tissue, and displaying only the blood vessel image<sup>[11]</sup>.

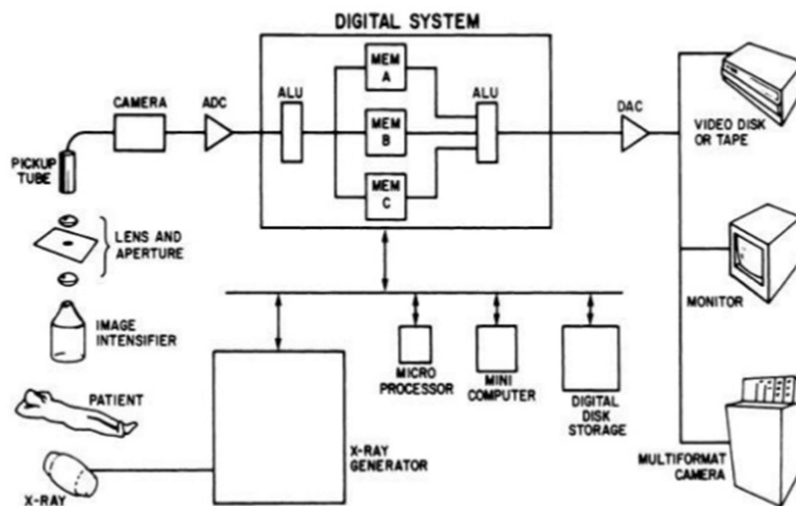


Figure 2. Structure of DSA system

DSA has better reproducibility than film angiography, which was mainly used in the past, and can freely change the contrast, so that even with a small amount of contrast agent, images of a certain contrast can be obtained. In addition, it is possible to change the image through real-time shooting, image storage, and post-processing. DAS requires an analog/digital converter that converts analog signals into digital signals, an image processor that processes and changes images, an image memory device and storage device that stores and stores images, and an image monitor<sup>[11]</sup>.

### 1. Experimental equipment

The equipment used in the experiment was DSA system from P company. There are two monitors used for the experiment by displaying angiographic images: P company's resolution 1280×1024 pixel monitor and W company's resolution 1536×2048 pixel monitor. MARO-viewer was used for PACS,

and analysis was performed by programming with Visual C++.

### 2. Experiment method

In the experiment, the quality of the sever image and the quality deterioration of the compressed and stored client image were compared, and the image quality of the monitor expressing the image was compared with the original. The evaluation image was used in the experiment using the DSA image acquired in the process of angiography.

### 3. Experimental procedure

In the experimental procedure, an angiography interventional procedure was performed, and the server image displayed on the monitor was acquired. And the same image was acquired by displaying it on the doctor's monitor. The two acquired images were programmed with Visual C++ to perform MSE and PSNR analysis.

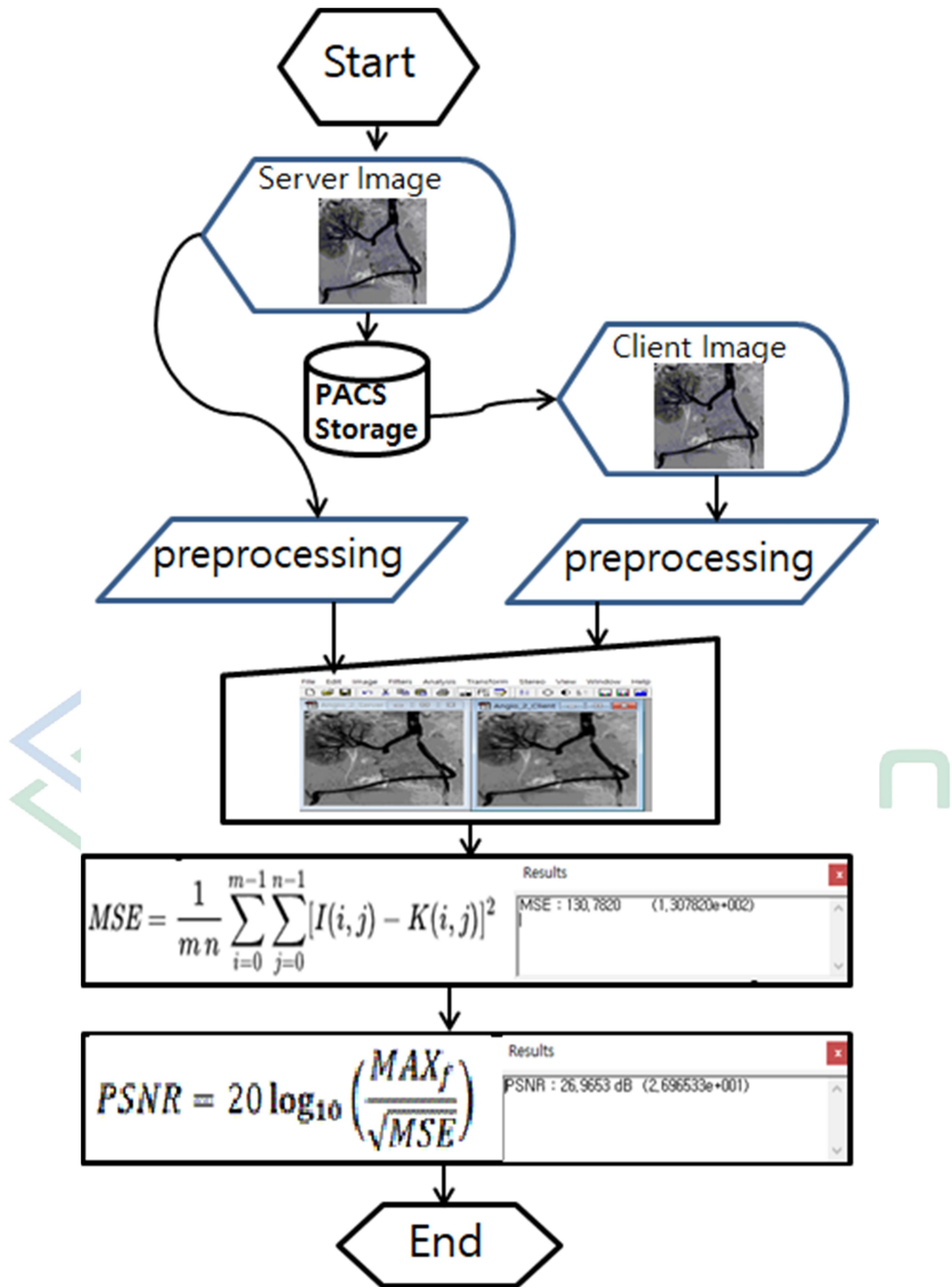


Figure 3. Experimental process

**3.1. An experiment images**

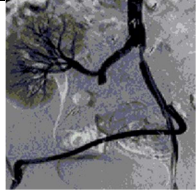
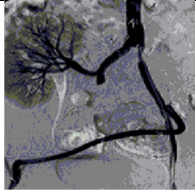
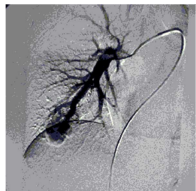
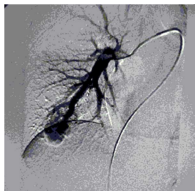
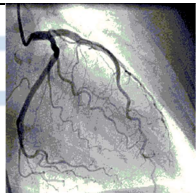
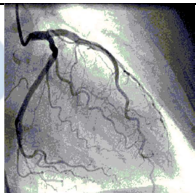




For the experiment, we acquired the server image in the

process of interventional angiography image. The monitor used at this time was a 1280×1024 pixel monitor from P’s company. And then, the image stored in the PACS server in the form of

\*.dcm was displayed on the PC of the doctor to obtain a client image. The monitor used at this time was a 1536×2048 pixel monitor from W's company. The acquired experimental images were Kidney angiography image, Lung angiography image,

Heart angiography image, Neck angiography image, and Knee angiography image. The obtained experimental images are shown in Table 1.

Table 1. Experimental images

No	Server image	Client image
1 Kidney angiography		
2 Lung angiography		
3 Heart angiography		
4 Neck angiography		
5 Knee angiography		

### 3.2. The Result of experiment

The experiment was carried out by the procedure

shown in Figure 3 by executing the experiment program. Table 2 shows the difference between the server image and the client. Table 3 shows the MSE and PSNR values obtained through the experiment.

Table 2. Difference between server image and client image







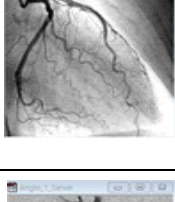




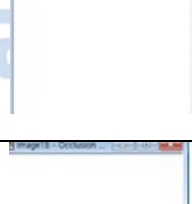
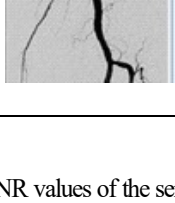
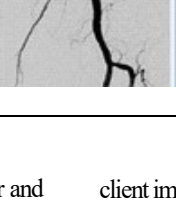
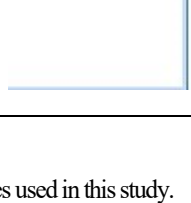
No	Server image	Client image	Difference image
1			
2			
3			
4			
5			

Table 3 shows the MSE and PSNR values of the server and client images used in this study.

Table 3. Result of experiment

No	MSE(Mean Square Error)	PSNR(Peak Signal-to-Noise Ratio)
1	130.7820	26.9553 [dB]
2	83.4332	28.9174 [dB]
3	338.7914	22.8315 [dB]
4	12.8791	37.0319 [dB]
5	3.1086	43.2052 [dB]



#### IV. Results and discussion

Looking at the difference between the two images shown in Table 2, there was a difference between the two images in images 1 to 3 in the body side, but no difference was found in images 4 and 5 in the neck and limb images. It can be seen that the MSE and PSNR values in Table 3 are also correlated with the difference between the two images.

The kidney angiography image of Table 3 number 1 showed a MSE value of 130.7820 and a PSNR value of 26.958 dB. The lung angiography image of Table 3 number 2 showed a MSE value of 83.4332 and a PSNR value of 28.9174 dB. The heart angiography image of Table 3 number 3 showed a MSE value of 338.7914 and a PSNR value of 22.8315 dB. The neck angiography image of Table 3 number 4 showed a MSE value of 12.8719 and a PSNR value of 37.0319 dB. The knee angiography image of Table 3 number 5 showed a MSE value of 3.1086 and a PSNR value of 43.2052 dB.

Changes in PSNR values of server and client images are considered to be a problem in resolution and management of server and client monitors, not in PACS image acquisition, storage, and transmission<sup>[12][13]</sup>.

#### V. Conclusion

In this study, PSNR analysis was performed on two images to evaluate the difference in the quality of images displayed on the server monitor and the client monitor in digital subtraction angiography.

The experiment tested the following 5 cases:

1. Kidney angiography image,
2. Lung angiography image,
3. Heart angiography image,
4. neck angiography image,
5. knee blood vessels image

As a result of the experiment, the PSNR value of the kidney

angiography image was 26.958dB, the PSNR value of the lung angiography image was 28.9174 dB, the PSNR value of the heart angiography image was 22.8315dB, and the PSNR value of the neck angiography image was 37.0319 dB, and the knee blood vessels image showed a PSNR value of 43.2052 dB, respectively.

In conclusion, it can be seen that there is almost no signal distortion in the process of acquiring, storing, and transmitting images in PACS. However, it suggests that the image signal may be distorted depending on the resolution and performance of each monitor. Therefore, it will be necessary to evaluate the performance of the monitor and to maintain the performance.

#### Competing interests

The authors declare that there is no conflict of interest regarding the publication of this paper

#### [Acknowledgment]

This study was supported by a National Research Foundation of Korea (NRF) grant funded by the Korean government (MEST) (NRF-2020R111A1A01060851).

#### [References]

- [1] Henning Kagermann, “*Change Through Digitization-Value Creation in the Age of Industry 4.0*”, Management of Permanent Change, PP. 23–45(2014)
- [2] Jake Luo, Min Wu, Deepika Gopukumar, et al, “*Big Data Application in Biomedical Research and Health Care: A Literature Review*”, Biomedical Informatics Insights, PMID: 6843812, DOI: 10.4137/BII.S31559 (2016)
- [3] Vibha Tiwari, P.P. Bansod, Abhay Kumar, “*Medical imaging in heterogeneous telemedicine network*”, IEEE, 2015 10<sup>th</sup> ICICS, Date of Conference: 2–4 Dec. 2015, INSPEC Accession Number: 15954747, DOI: 10.1109/ICICS.2015.7459982
- [4] Israna Hossain Arka, Kalaivani Chellappan, “*Collaborative Compressed I-cloud Medical Image Store with Decompress Viewer*”, Procedia Computer

- Science, Vol. 42, PP. 114~121(2014)
- [5] C. J. Martin, P. E. Sharp, D. G. Sutton, "**Measurement of image quality in diagnostic radiology**", Applied Radiation and Isotope, Vol. 50, Issue 1, PP. 21~38(1999)
- [6] L. P. Yaroslavsky, "**Compression, restoration, resampling, 'compressive sensing': fast transforms in digital imaging**", Journal of Optics, Vol. 17, No. 7 TOPICAL REVIEW (2015)
- [7] Zhou Wang, A. C. Bovik, "**A universal image quality index**", IEEE Signal Processing Letters, Vol. 9, Issue 3, PP. 81~84(2002)
- [8] Seema Rajput, S.R.Suralkar, "**Comparative Study of Image Enhancement Techniques**", IJCSMC, Vol. 2, Issue 1, PP. 11~21(2013)
- [9] Elizabeth A, Krupinski, "**Current perspectives in medical image perception**", Atten Percept Psychophys, Vol. 72, No. 5(2010), doi : 10.3758/APP.72.5.1205
- [10] Quan Huynh-Thu, Mohammed Ghanbari, "**The accuracy of PSNR in predicting video quality for different video scenes and frame rates**", Telecommunication Systems, Vol. 49, No. 1, PP. 35~48(2012)
- [11] William R. Brody, "**Digital Subtraction Angiography**", IEEE Transactions on Nuclear Science, Vol. 29, Issue 3, PP. 1176~1180(1982)
- [12] Iza Sazanita Isa, Siti Noraini Sulaiman, Muzaimi Mustapha, Sailudin Darus, "**Evaluating Denoising Performance of Fundamental Filters for T2-Weighted MRI Images**", Procedia Computer Science, Vol. 60, pp. 760~768(2015)
- [13] Pavel Morozkin, "**Design and implementation of image processing and compression algorithms for a miniature embedded eye tracking system**", HAL, Signal and Image processing. Sorbonne Université, 2018

# Analysis of Fitting Degree of MRI and PET Images in Simultaneous MR-PET Images by Machine Learning Neural Networks

<sup>1</sup>GilJae Lee, <sup>1\*</sup>Hwunjae Lee, <sup>2\*</sup>Gyehwan Jin

Received: 27 August 2020 / Accepted: 22 November 2020 / Published online: 28 December 2020

©The Author(s) 2020

**Abstract** Simultaneous MR-PET imaging is a fusion of MRI using various parameters and PET images using various nuclides. In this paper, we performed analysis on the fitting degree between MRI and simultaneous MR-PET images and between PET and simultaneous MR-PET images. For the fitness analysis by neural network learning, feature parameters of experimental images were extracted by discrete wavelet transform (DWT), and the extracted parameters were used as input data to the neural network. In comparing the feature values extracted by DWT for each image, the horizontal and vertical low frequencies showed similar patterns, but the patterns were different in the horizontal and vertical high frequency and diagonal high frequency regions. In particular, the signal value was large in the T1 and T2 weighted images of MRI. Neural network learning results for fitting degree analysis were as follows.

1. T1-weighted MRI and simultaneous MR-PET image fitting degree: Regression (R) values were found to be Training 0.984, Validation 0.844, and Testing 0.886.
2. Dementia-PET image and Simultaneous MR-PET Image fitting degree: R values were found to be Training 0.970, Validation 0.803, and Testing 0.828.
3. T2-weighted MRI and concurrent MR-PET image fitting degree: R values were found to be Training 0.999, Validation 0.908, and Testing 0.766.
4. Brain tumor-PET image and Simultaneous MR-PET image fitting degree: R values were found to be Training 0.999, Validation 0.983, and Testing 0.876.

An R value closer to 1 indicates more similarity. Therefore, each image fused in the simultaneous MR-PET images verified in this study was found to be similar. Ongoing study of images acquired with pulse sequences other than the weighted images in the MRI is needed. These studies may establish a useful protocol for the acquisition of simultaneous MR-PET images.

<sup>1</sup>GilJae Lee

Business Promotion Agency, Chungbuk Technopark  
(28116)40, Yeongudanji-ro, Cheongju-si,  
Chungcheongbuk-do, Korea

<sup>1\*</sup>Hwunjae Lee

Department of Radiology, College of Medicine  
(03722)Yonsei University, 50-1, Yonsei-ro, Seodaemoon-  
gu, Seoul, Korea  
YUHS-KRIBB Medical Convergence Research Institute,  
College of Medicine, Yonsei University, Seoul, Korea

<sup>2\*</sup>Gyehwan Jin (✉) *corresponding author*

Dept. of Radiology, Nambu University  
(62271)Department of Radiology, Nambu University 23  
Chumdan Jungang-ro, Gwangsan-gu, Gwangju, Korea

**Keywords:** Simultaneous MR-PET, Medical image registration, Feature extraction, Artificial intelligence, Neural networks

## I. Introduction

The discovery of x-rays provided a way to see inside the human body for the first time in history and has been an opportunity for the

development of modern medicine [1]. In the late 20th century, advanced imaging techniques such as computed tomography (CT), magnetic resonance imaging (MRI), and positron emission tomography (PET) were developed by grafting computer technology to medical imaging equipment. These medical imaging devices enable evaluation of the anatomy and physiological characteristics of the human body and can express these characteristics in 3D high resolution [2]. The simultaneous MR-PET examination can obtain images of higher soft tissue contrast while exposing the patient to less radiation compared with the PET-CT examination. The reason is that 70% of radiation exposure in PET/CT scans is from CT, and MRI has higher soft tissue contrast than CT [3]. Therefore, simultaneous MR-PET testing is advantageous for testing patients of reproductive age, children, and pregnant women [3]. Simultaneous MR-PET acquires an image in one session and completely registers anatomical and functional information. In contrast, sequential PET-MRI may cause resampling and registration errors between the PET scan and the MRI scan by sequentially performing two scans. In addition, the sequential PET-MRI examination increases the examination time, causing inconvenience to the patient. From a technical point of view, patient motion is a major problem with whole-body PET scans and affects image quality and quantification [3]. Simultaneous MR-PET scans are integrated into the modeling and PET reconstruction process to provide accurate motion measurements that can produce motion-free PET images [3].

In this paper, we evaluated whether the fusion image acquired by simultaneous MR-PET was properly mapped (fitting degree) to the characteristics of the PET image and the characteristics of the MRI. In the evaluation, after segmenting the experimental image, features were extracted by DWT, and the extracted feature values were used as input signals to the neural network to be evaluated by machine learning.

## II. Materials and Methods

### 1. Simultaneous MR-PET images

Simultaneous MR-PET is a method that can simultaneously perform PET using radiopharmaceuticals that emit positrons and MRI using superconducting magnets and radio high frequency [7]. Simultaneous MR-PET is a fusion molecular imaging system that combines PET that shows ultra-sensitive molecular images and MRI capable of high-resolution functional imaging. It has the advantages of improved diagnostic accuracy compared with xxx, aids in developing new imaging biomarkers and new drugs, reduced radiation exposure, and improved patient convenience [7]. Compared with PET-CT, PET-MRI exposes patients to less radiation (up to 70% of the dose received from PET-CT scans is due to CT) and has a higher contrast for soft tissue [5]. Since simultaneous MR-PET is an all-in-one device, it acquires two examinations at the same time, reducing the examination time by almost half compared with the device that acquires PET and MRI in sequence [7]. Therefore, the accuracy of the examination, patient convenience, and the profitability of the equipment are increased. For example, due to simultaneous acquisition, errors due to movement are minimized, thereby increasing the accuracy of diagnosis around a moving bowel and a bladder filled with urine. In simultaneous MR-PET, measurements can be performed in one single session, but separate scanners have to adjust the two examinations, which further affects the overall examination time and patient comfort [7]. Simultaneous MR-PET can provide complete registration with anatomical and functional information, but sequential PET-MRI can cause errors due to resampling and registration between PET and MRI images. Simultaneous MRI scans are integrated into the modeling and PET reconstruction process to provide accurate motion measurements that can produce motion-free PET images [7]. PET also provides quantitative functional information as long as certain data modifications, such as attenuation and scattering of  $\gamma$  photons in patient tissue, are applied correctly. CT provides contrast information for X-ray absorption based on the electron density of the tissue, whereas MRI provides contrast information for the proton density of tissue [8]. Other strategies for converting proton density to electron density in specific cases of brain PET have been studied [9].

The combination of PET and MRI requires significant advances in the software that supports the

measurement of signals such as the influence of the magnetic field by the superconducting magnet of the MRI, attenuation and motion compensation, and

design errors in the new RF coil on the PET amplification device [7].

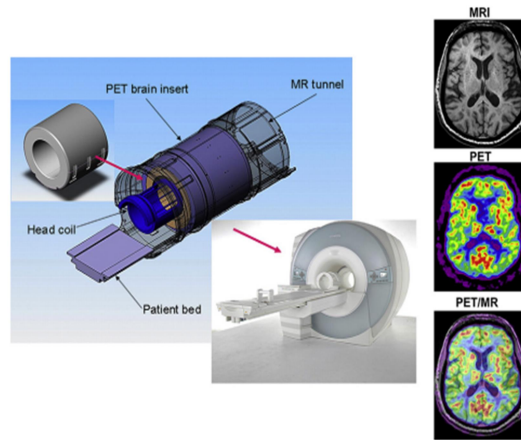


Figure 1. Simultaneous MR-PET diagram and images<sup>[4]</sup>

## 2. Feature extraction of simultaneous MR-PET images by discrete wavelet transform (DWT)

Wavelet transforms can construct a model of a signal, system, or process into a specific set of signals [10]. This special signal is called a wavelet, and it is expressed as an arbitrary waveform through a localized small wavelet as a pattern and is transformed, enlarged, or reduced. The characteristic of time-frequency analysis by wavelet transformation

is that the time resolution is high in the high-frequency domain and the frequency resolution is high in the low-frequency domain [10]. The two-dimensional wavelet decomposition algorithm of the image works similarly to the one-dimensional case. The two-dimensional wavelet and scaling function are obtained by taking the tensor product and scaling function of the one-dimensional wavelet.

This kind of two-dimensional DWT decomposes the approximation coefficient at level  $j$  into four components, the approximation at level  $j + 1$  and the detail in three directions (horizontal, vertical, and diagonal) [10]. [Figure 2] explains the decomposition step [11].

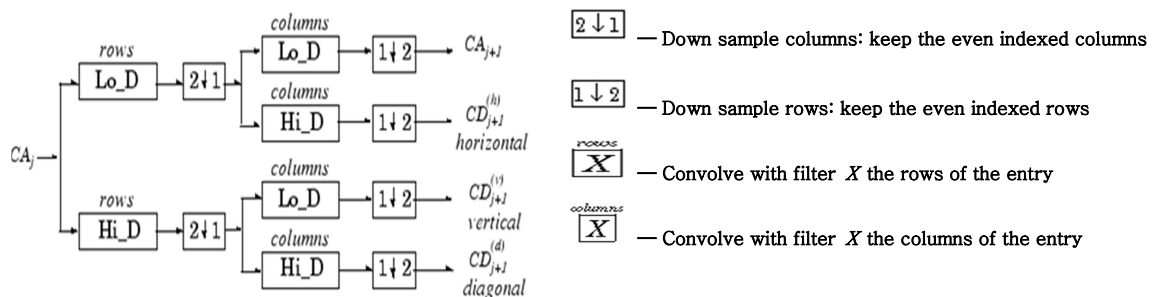


Figure 2. Decomposition step of the image by DWT<sup>[11]</sup>

### 3. Self-organizing maps (SOM)

The feature mapping of the structure of a self-organizing neural network is the transformation of input patterns of any dimension into outputs of neurons composed of a one-dimensional or two-dimensional array. The neural network that performs these ideas is called a feature map [12]. In addition to dimensional reduction, feature maps also have features that preserve topology. That is, input

patterns that are close to each other activate output units that are close to each other in the feature map. This is also an important feature of feature maps found in the cerebral cortex of developed animals [12]. SOM is generally composed of a one-dimensional or two-dimensional array of units, and each unit is connected to all  $n$  input nodes. If the  $n$ -dimensional vector of the unit in  $(i, j)$  is  $w_{ij}$ , each neuron calculates the Euclidean distance between the input vector and the stored connection strength vector  $w_{ij}$  [12][13].

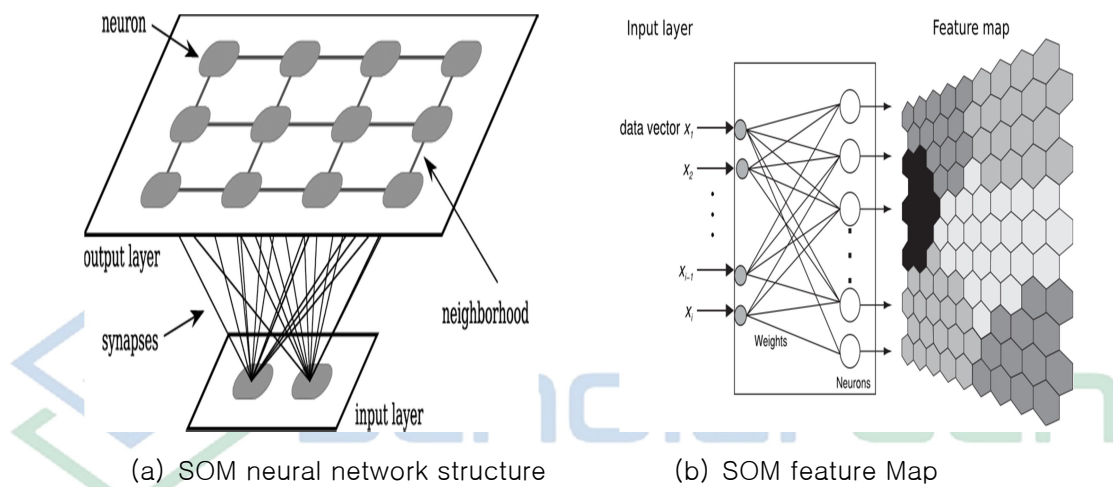


Figure 3. Self-Organizing Maps (SOM)<sup>[12][13]</sup>

### III. Experimental Results and Discussion

The experiment was performed following the experimental concept diagram in [Figure 4]. The fitting degree of the MR and PET images of the simultaneous MR-PET image of (2) acquired with the equipment (1) in [Figure 4] was analyzed. In step (3), each image (MRI, PET, simultaneous MR-PET

image) for the experiment was subjected to DWT. Low-frequency coefficient matrix  $6 \times 16$  feature parameters were extracted with the 3-step DWT. The extracted parameters were input to the SOM neural network configured in (4) and the result was obtained in (5).



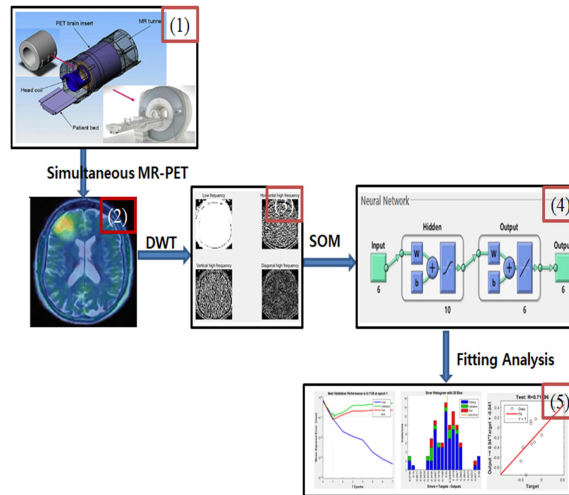


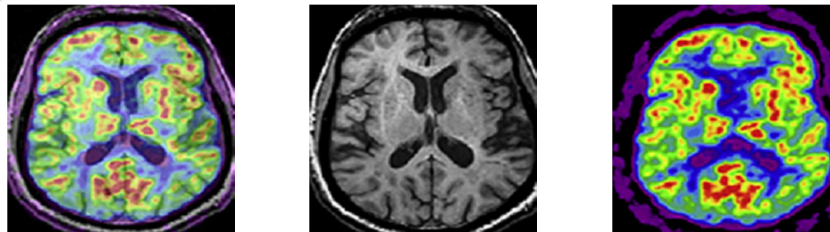
Figure 4. Experimental procedure

**1. Image acquisition and preprocessing**

Figure 5 and Figure 6 show the medical images used in the experiment. The experimental image was adjusted to 256 X 256 pixels, and the image shape was pre-processed in the form of a bit map (\*.bpm).

To extract the features of the experimental image, we implemented and executed the DWT program using Matlab R2015. The experiment was conducted with the SOM neural network using the extracted features as input.

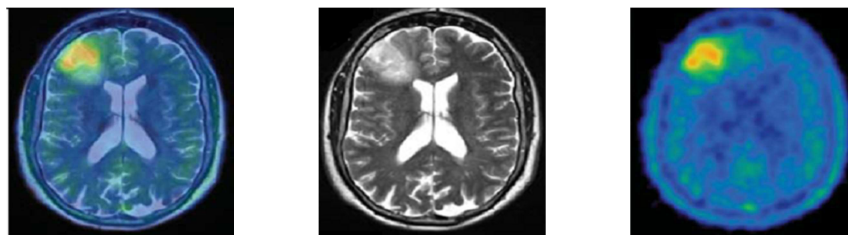
**A. T1-weighted MRI and Dementia PET fusion image**



(a) Fusion Image (b) T1-weighted MRI (c) Dementia PET Image

Figure 5. T1-weighted MRI and Dementia PET fusion images

**B. T2-weighted MRI and brain tumor PET fusion image**



(a) Fusion Image (b) T2-wighted MRI Brain tumor PET Image

Figure 6. T2-weighted MRI and brain tumor PET fusion images

## 2. DWT

Matlab M-Programming was performed for DWT. The experimental images were performed by pre-processing the six images in Figures 5 and 6 into 256 X 256 pixels and then segmenting the disease area.

## fusion image

[Table 1] shows the 6 X 16 matrix feature extraction values obtained as a result of 3-step DWT after the segmentation of a simultaneous MR-PET (T1WI and Dementia PET fusion image) image.

### A. T1-weighted MRI (T1WI) and Dementia PET

Table 1. Feature extraction results of Simultaneous MR-PET (T1WI and Dementia PET fusion image)

Features of T1-weighted MRI and Dementia PET fusion image																
A4H	-0.50	-0.50	-0.50	-0.49	-0.48	-0.48	-0.18	0.15	0.29	0.35	0.40	0.42	0.47	0.49	0.50	0.50
A4V	-0.50	-0.50	-0.50	-0.49	-0.44	-0.11	0.13	0.25	0.35	0.40	0.48	0.48	0.47	0.50	0.38	0.43
H4V	-0.50	-0.50	-0.48	-0.40	-0.41	0.11	0.50	-0.07	-0.16	-0.39	-0.36	-0.44	-0.43	-0.44	-0.42	-0.45
V4H	-0.50	-0.50	-0.49	-0.25	0.50	0.01	-0.17	-0.29	-0.41	-0.42	-0.28	-0.22	-0.47	-0.37	-0.30	-0.22
D4H	-0.50	-0.50	-0.49	-0.40	-0.33	0.50	0.38	0.00	0.04	-0.40	-0.28	-0.30	-0.30	-0.41	-0.37	-0.42
D4V	-0.50	-0.50	-0.48	0.03	0.50	0.10	0.07	0.07	-0.25	-0.09	0.16	0.02	-0.44	-0.24	-0.04	0.10

#### 1) Feature extraction of T1WI

[Table 2] shows the 6 X 16 matrix feature extraction

values obtained as a result of 3-step DWT after the segmentation of T1WI.

Table 2. Feature extraction results of T1-weighted MRI

Features of T1-weighted MRI																
A4H	-0.50	-0.48	-0.28	-0.18	-0.10	-0.26	-0.12	0.06	0.14	0.14	0.24	0.29	0.39	0.47	0.50	0.34
A4V	-0.50	-0.49	-0.47	-0.45	-0.24	-0.08	0.06	0.25	0.34	0.47	0.50	0.27	0.40	0.42	0.33	0.42
H4V	-0.50	0.26	0.33	0.35	0.50	0.29	-0.05	-0.28	-0.13	-0.07	-0.09	-0.09	-0.17	-0.23	-0.09	0.17
V4H	-0.50	-0.19	0.05	0.26	0.34	0.37	0.03	0.43	-0.16	0.08	0.50	0.42	0.26	0.42	0.14	0.43
D4H	-0.50	-0.10	0.22	0.34	0.41	0.06	0.50	0.38	0.09	0.15	0.35	-0.09	-0.09	-0.14	0.27	0.20
D4V	-0.50	-0.24	0.11	0.08	0.07	0.25	-0.16	0.05	-0.30	0.11	0.12	0.50	0.07	-0.13	-0.10	0.22

Each parameter (A4H, A4V, V4H, H4V, D4H, D4V) in [Table 1] and [Table 2] containing the feature extraction values obtained by DWT is shown as a graph. [Figure 7] shows graphs of A4H (horizontal low-frequency characteristics) and A4V (vertical

low-frequency characteristics) in [Table 1] and [Table 2]. The results show that the characteristics of the vertical and horizontal low-frequency regions are similar.

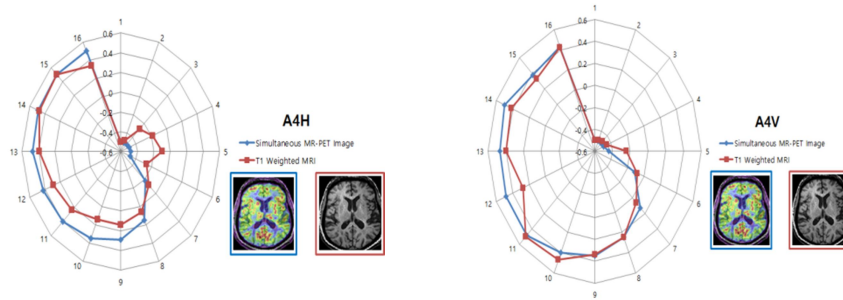


Figure 7. A4H (horizontal low frequency characteristics) and A4V (vertical low-frequency characteristics) graph in [Table 1] and [Table 2]

[Figure 8] shows graphs of H4V (horizontal high-frequency feature) and V4H (vertical high-frequency feature) in [Table 1] and [Table 2]. The characteristics of the vertical and horizontal high-

frequency regions are different, and the results show that the T1WI image contains many high-frequency components.

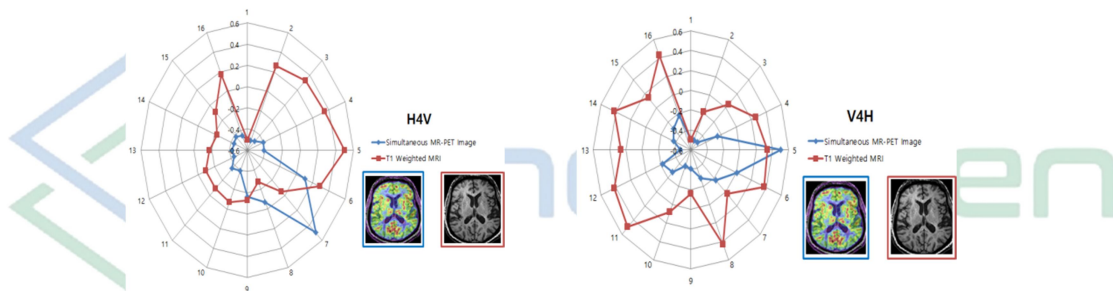


Figure 8. H4V (horizontal high frequency characteristic) and V4H (vertical high frequency characteristic) graph in [Table 1] and [Table 2]

[Figure 9] shows graphs of D4H (diagonal high-frequency characteristics) and D4V (diagonal low-frequency characteristics) in [Table 1] and [Table 2]. The characteristics of the frequency domain in the

diagonal direction are different, and the results show that the T1WI image has many frequency components.

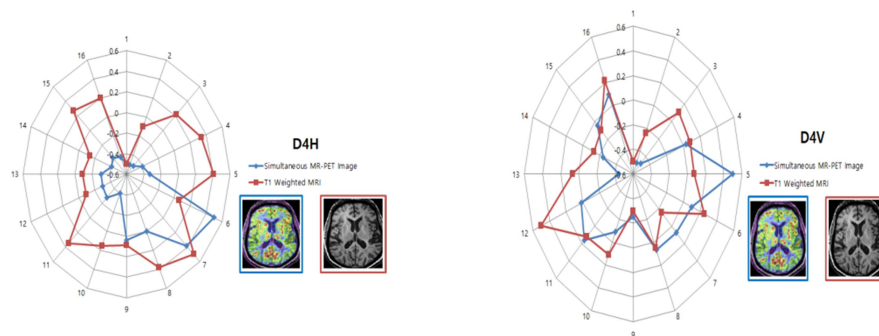


Figure 9. D4H (diagonal high frequency characteristics) and D4V (diagonal low frequency characteristic) graph in [Table 1] and [Table 2]

**2) Feature extraction of Dementia PET image**

[Table 3] shows the 6 X 16 matrix feature extraction

values obtained as a result of 3-step DWT after segmentation of the Dementia-PET image.

Table 3. Feature extraction results of Dementia PET image

Features of Dementia PET image																
A4H	-0.50	-0.50	-0.50	-0.50	-0.50	-0.50	-0.46	-0.07	0.09	0.22	0.36	0.41	0.45	0.48	0.49	0.50
A4V	-0.50	-0.50	-0.50	-0.50	-0.48	-0.21	0.08	0.22	0.32	0.40	0.47	0.50	0.48	0.50	0.26	0.44
H4V	-0.50	-0.50	-0.50	-0.50	-0.50	-0.38	0.50	0.12	0.09	-0.10	-0.42	-0.40	-0.43	-0.48	-0.43	-0.48
V4H	-0.50	-0.50	-0.50	-0.44	0.49	0.37	-0.02	-0.11	-0.24	-0.42	-0.42	-0.44	-0.39	0.50	0.21	-0.29
D4H	-0.50	-0.50	-0.50	-0.50	-0.50	-0.31	0.50	-0.09	0.17	0.04	-0.26	-0.23	-0.40	-0.48	-0.35	-0.45
D4V	-0.50	-0.50	-0.50	-0.48	0.11	0.50	0.09	0.18	-0.19	0.02	-0.24	-0.38	-0.21	0.26	0.07	-0.06

[Figure 10] shows graphs of A4H (horizontal low frequency characteristics) and A4V (vertical low frequency characteristics) in [Table 1] and [Table 3].

The results show that the characteristics of the vertical and horizontal low frequency regions are similar.

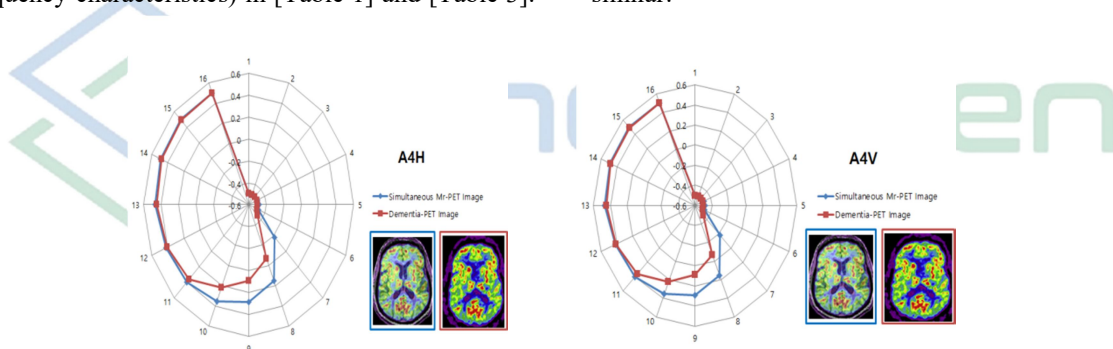


Figure 10. A4H (horizontal low frequency characteristics) and A4V (vertical low-frequency characteristics) graph in [Table 1] and [Table 3]

[Figure 11] is a graph showing H4V (horizontal high frequency characteristics) and V4H (vertical high frequency characteristics) in [Table 1] and [Table 3]. The results show that the characteristics of

the vertical and horizontal high-frequency regions are different and that the Dementia-PET image has more high-frequency components.

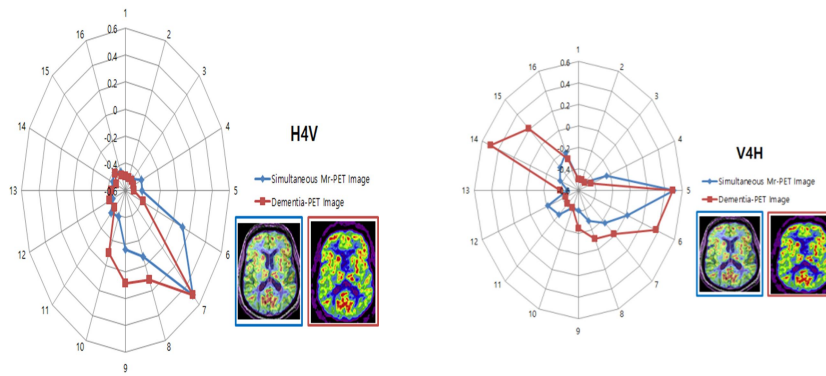


Figure 11. H4V (horizontal high frequency characteristic) and V4H (vertical high frequency characteristic) graph in [Table 1] and [Table 3]

[Figure 12] shows graphs of D4H (diagonal high-frequency characteristics) and D4V (diagonal low-frequency characteristics) in [Table 1] and [Table 3].

The results show that the characteristics of the diagonal high-frequency region are similar.

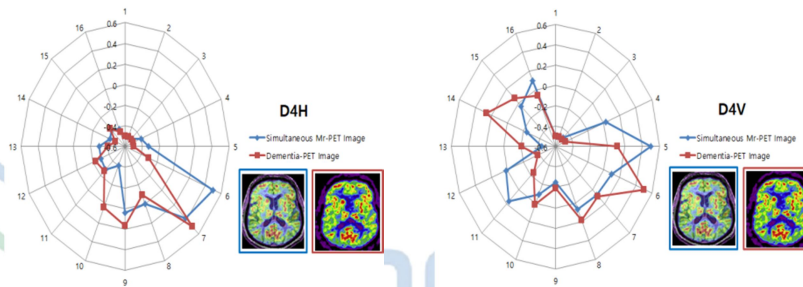


Figure 12. D4H (diagonal high frequency characteristics) and D4V (diagonal low frequency characteristic) graph in [Table 1] and [Table 3]

**B. T2-weighted MRI (T2WI) and brain tumor PET fusion image**

values obtained as a result of 3-step DWT after segmentation of simultaneous MR-PET (T2WI and Brain tumor-PET fusion image) images.

[Table 4] shows the 6 X 16 matrix feature extraction

Table 4. Feature extraction results of Simultaneous MR-PET (T2WI and brain tumor PET fusion image) image

Features of T2-weighted MRI and brain tumor PET fusion image																
A4H	-0.50	-0.50	-0.50	-0.50	-0.50	-0.50	-0.47	-0.29	-0.38	-0.10	0.11	0.34	0.50	0.44	0.17	-0.29
A4V	-0.50	-0.50	-0.50	-0.49	-0.45	-0.37	-0.02	0.28	0.44	0.50	0.38	0.10	-0.36	-0.38	-0.42	-0.46
H4V	-0.50	-0.50	-0.48	-0.50	-0.50	-0.48	0.22	-0.04	0.09	-0.23	-0.33	-0.38	-0.37	0.00	0.50	0.36
V4H	-0.50	-0.50	-0.50	-0.28	0.26	0.08	0.15	-0.14	-0.05	0.12	0.50	0.45	0.10	0.17	-0.20	-0.33
D4H	-0.50	-0.50	-0.43	-0.48	-0.50	-0.47	0.41	0.45	0.28	-0.04	0.28	-0.04	-0.12	0.38	0.50	0.50
D4V	-0.50	-0.50	-0.50	-0.16	0.02	0.48	0.11	-0.14	-0.01	0.35	0.50	0.36	0.14	0.37	-0.32	-0.24

**1) Feature extraction of T2WI**

[Table 5] shows the 6 X 16 matrix feature extraction values obtained as a result of 3-step DWT after

segmentation of T2WI.

Table 5. Feature extraction results of T2WI

Features of T2-weighted MRI																
A4H	-0.50	-0.49	-0.42	-0.38	-0.45	-0.35	-0.24	-0.10	0.06	0.08	0.24	0.41	0.50	0.29	0.09	-0.01
A4V	-0.50	-0.50	-0.50	-0.47	-0.29	-0.08	0.05	0.29	0.38	0.50	0.37	0.24	-0.24	-0.13	-0.26	-0.30
H4V	-0.50	-0.29	0.06	-0.30	-0.08	0.50	0.44	0.14	-0.16	-0.25	-0.28	-0.42	-0.17	-0.12	0.06	-0.03
V4H	-0.50	-0.50	-0.50	0.06	0.50	0.08	-0.19	-0.28	-0.18	0.14	-0.01	0.25	0.26	0.17	0.01	-0.37
D4H	-0.50	-0.43	-0.38	-0.23	-0.06	-0.03	0.50	0.25	-0.06	-0.08	-0.12	-0.43	-0.18	-0.22	-0.18	0.12
D4V	-0.50	-0.50	-0.49	-0.26	-0.10	0.50	0.04	0.27	0.26	0.37	0.26	0.02	0.00	0.13	0.17	0.04

[Figure 13] shows graphs of A4H (horizontal low frequency characteristics) and A4V (vertical low frequency characteristics) in [Table 4] and [Table 5].

The results show that the characteristics of the low frequency region are similar.

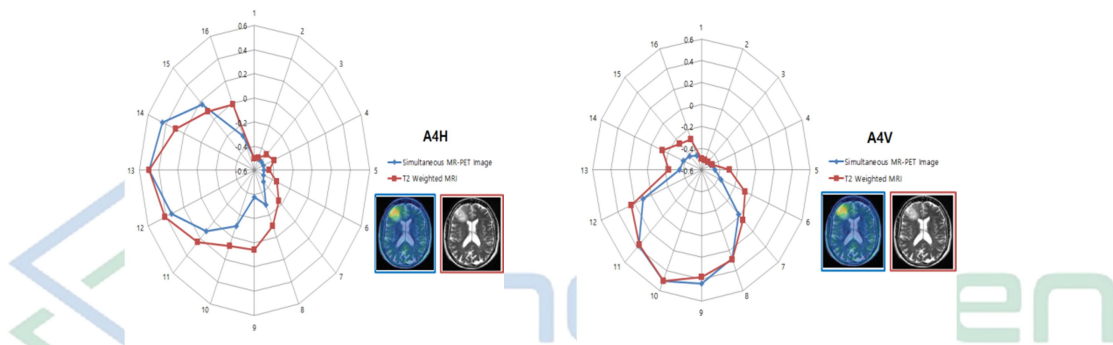


Figure 13. A4H (horizontal low frequency characteristics) and A4V (vertical low-frequency characteristics) graph in [Table 4] and [Table 5]

[Figure 14] shows graphs of H4V (horizontal high frequency characteristics) and V4H (vertical high frequency characteristics) in [Table 4] and [Table 5].

The results show that the characteristics of the high-frequency region are less than that of the low-frequency region, but are similar.

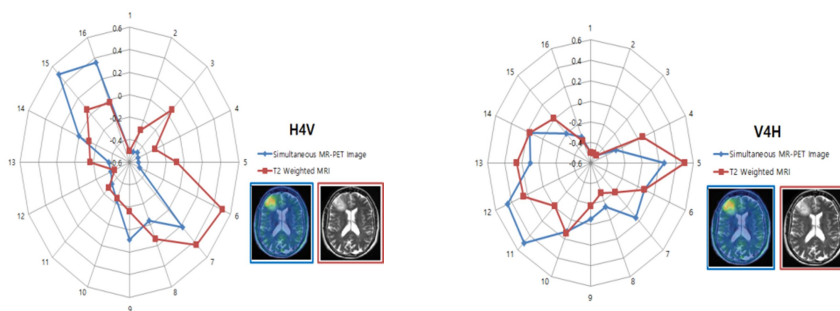


Figure 14. H4V (horizontal high frequency characteristic) and V4H (vertical high frequency characteristic) graph in [Table 4] and [Table 5]

[Figure 15] shows graphs of D4H (diagonal high-frequency characteristics) and D4V (diagonal low-

frequency characteristics) in [Table 4] and [Table 5]. The results show that the characteristics of the



diagonal high-frequency region are less than that of the low-frequency region, but are similar.

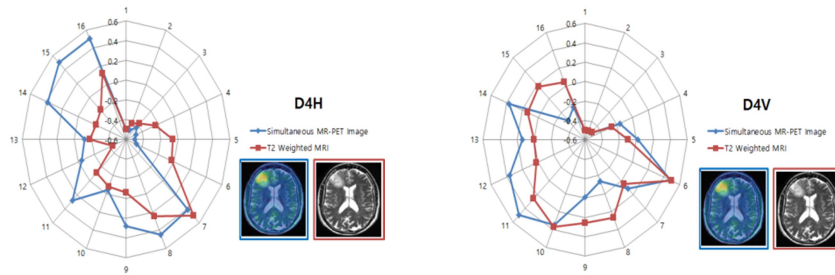


Figure 15. D4H (diagonal high frequency characteristics) and D4V (diagonal low frequency characteristic) graph in [Table 4] and [Table 5]

**2) Feature extraction of brain tumor PET image**

values obtained as a result of 3-step DWT after segmentation of a brain tumor-PET image.

[Table 6] shows the 6 X 16 matrix feature extraction

Table 6. Feature extraction results of brain tumor PET image

Features of brain tumor PET image																
A4H	-0.50	-0.50	-0.50	-0.50	-0.50	-0.50	-0.50	-0.50	-0.47	-0.10	0.30	0.50	0.43	0.41	0.30	-0.43
A4V	-0.50	-0.50	-0.50	-0.50	-0.50	-0.47	0.03	0.32	0.42	0.50	0.00	-0.50	-0.50	-0.50	-0.50	-0.50
H4V	-0.50	-0.50	-0.50	-0.50	-0.50	-0.50	-0.50	-0.41	0.29	0.26	0.04	-0.36	-0.41	0.20	0.50	-0.32
V4H	-0.50	-0.50	-0.50	-0.50	-0.41	-0.18	-0.20	-0.33	-0.38	0.50	0.26	-0.49	-0.50	-0.50	-0.50	-0.50
D4H	-0.50	-0.50	-0.50	-0.50	-0.50	-0.50	-0.50	-0.45	-0.28	0.50	0.14	-0.26	-0.46	0.24	0.19	-0.42
D4V	-0.50	-0.50	-0.50	-0.50	-0.45	0.33	0.50	0.03	-0.14	0.39	-0.17	-0.48	-0.50	-0.50	-0.50	-0.50

[Figure 16] shows graphs of A4H (horizontal low frequency features) and A4V (vertical low frequency features) in [Table 4] and [Table 6]. The results show

that the characteristics of the low frequency region are similar.

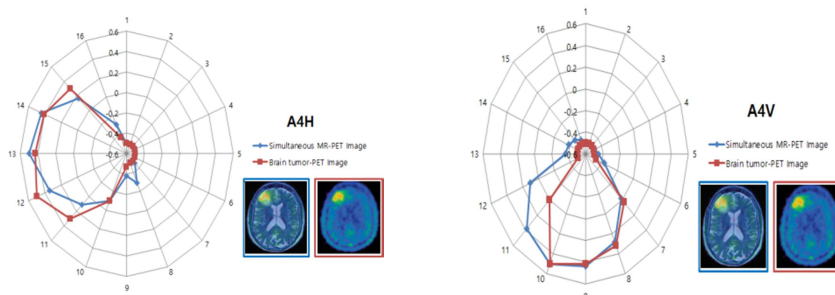


Figure 16. A4H (horizontal low frequency characteristics) and A4V (vertical low-frequency characteristics) graph in [Table 4] and [Table 6]

[Figure 17] is a graph showing H4V (horizontal high frequency feature) in [Table 4] and [Table 6] and V4H (vertical high frequency feature) in [Table 4]

and [Table 6]. The results show that the characteristics of the horizontal and vertical high frequency regions are different.

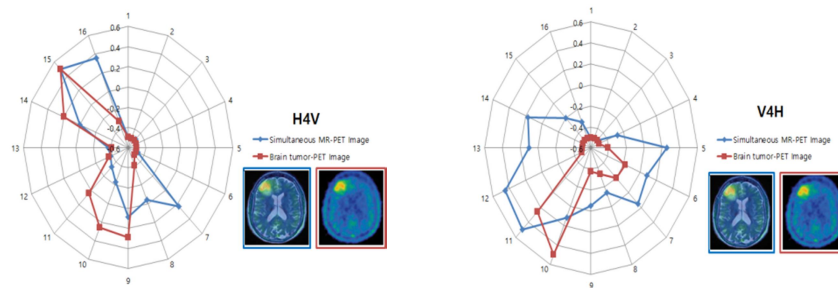


Figure 17. H4V (horizontal high frequency characteristic) and V4H (vertical high frequency characteristic) graph in [Table 4] and [Table 6]

[Figure 18] is a graph showing D4H (diagonal high-frequency characteristics) and D4V (diagonal low-frequency characteristics) in [Table 4] and [Table 6].

The results show that the characteristics of the diagonal high-frequency regions are different.

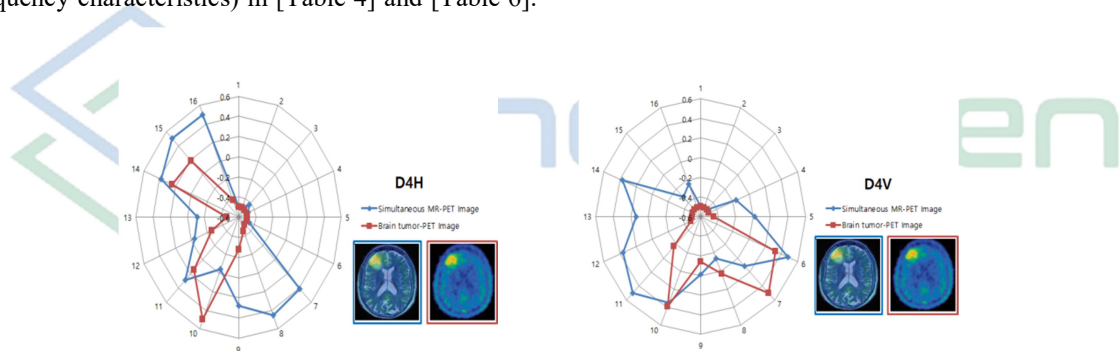


Figure 18. D4H (diagonal high frequency characteristics) and D4V (diagonal low frequency characteristic) graph in [Table 4] and [Table 6]

### 3. Neural network machine learning

[Figure 19] is a model diagram of a neural network for this experiment. The input variables are

sequentially input 16 times with 6 extracted feature values, and learned, 10 hidden layers, 6 output layers, and 6 output values.

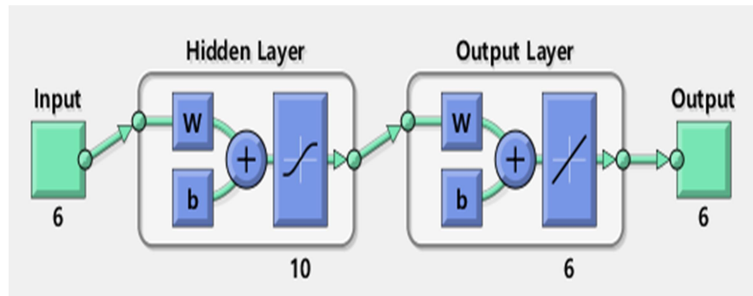


Figure 19. Neural Networks

The Levenberg-Marquardt algorithm (LMA or LM), also known as the damped least squares (DLS) method in mathematics and computing, is used to solve nonlinear least-squares problems [14][15]. This minimization problem especially arises in the least-squares curve fitting. This algorithm usually uses more memory but takes less time. When the generalization improvement stops as the mean squared error of the validation sample increases, learning is automatically stopped. In learning, the mean squared error is the mean squared difference between the output and the target [9]. A lower value is better, and 0 means no error. The regression R-value measures the correlation between the output and the target. An R-value of 1 means a close relationship, while an R-value of 0 means a random relationship [14][15].

**1) Fitting degree of T1WI and simultaneous MR-PET images**

[Figure 19] The T1WI feature value in [Table 2] was input as the input data of the neural network; for target data, the simultaneous MR-PET (T1WI and Dementia PET fusion image) feature values in [Table 1] were input. During learning, the mean squared error (MSE) is the mean squared difference between the output and the target [14]. A smaller value indicates fewer errors. The regression R-value is a measure of the correlation between the output and the target. If the R-value is close to 1, the relationship is close [14][15]. [Table 7] shows that the R-value is close to 1 for all of the training, validation, and testing, indicating that the T1WI and simultaneous MR-PET images are well fit.

**A. T1WI and Dementia PET fusion image**

Table 7. Result of neural network machine learning (T1-weighted MRI and simultaneous MR-PET images)

	Sample	MSE	R
Training	12	5.00E-03	9.9999E-01
Validation	2	2.96E-02	8.4422E-01
Testing	2	3.70E-02	8.85649E-01

[Figure 20] is a graph showing the regression.

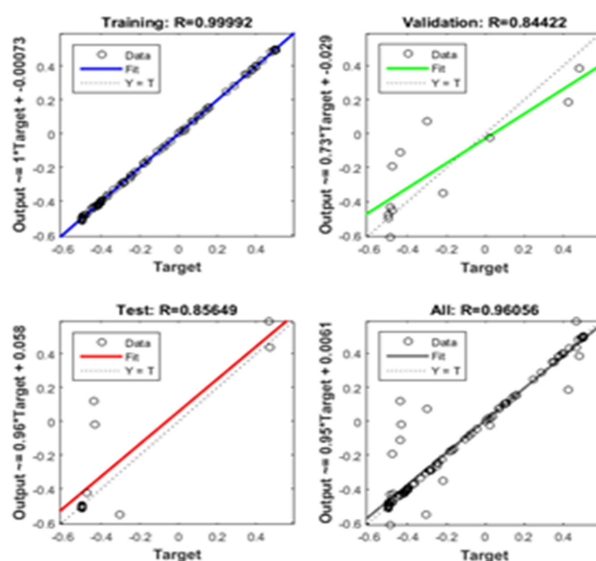


Figure 20. Regression graph (T1-weighted MRI and simultaneous MR-PET images)

## 2) Fitting degree of dementia PET image and simultaneous MR-PET images

[Figure 19] For the input data of the neural network, the characteristic values of the Dementia-PET image in [Table 3] were input; for the target data, the simultaneous MR-PET (T1WI and

Dementia PET fusion image) feature values in [Table 1] were input. [Table 8] shows that the R-value is close to 1 for all of the training, validation, and testing, indicating that the Dementia-PET image and the simultaneous MR-PET image are fitting.

Table 8. Result of neural network machine learning (dementia PET image and simultaneous MR-PET images)

	Sample	MSE	R
Training	12	5.91E-03	9.7027E-01
Validation	2	2.89E-02	8.0298E-01
Testing	2	5.15E-02	8.2837E-01

[Figure 21] is a graph showing regression.

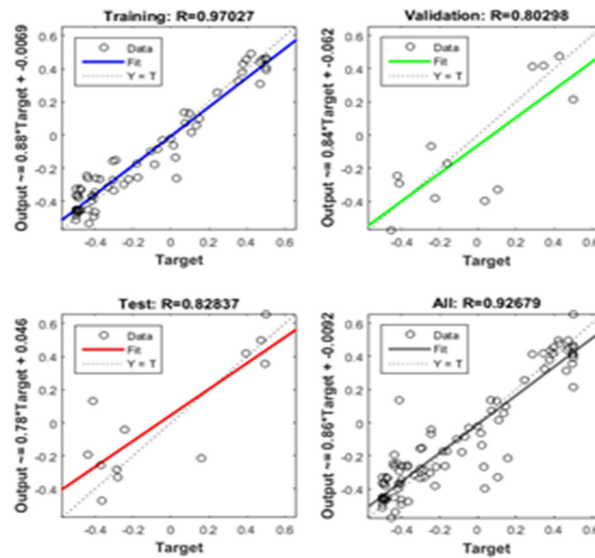


Figure 21. Regression graph (dementia PET image and simultaneous MR-PET images)

**B. T2WI and brain tumor PET fusion image**

**1) Fitting degree of T2WI and simultaneous MR-PET images**

[Figure 19] For the input data of the neural network, the T2WI feature values in [Table 5] were

input; for the target data, the simultaneous MR-PET (T2WI and Brain tumor-PET fusion image) feature values in [Table 4] were input. [Table 9] shows that the R-value is close to 1 in all of the training, validation, and testing, indicating that the T2WI and simultaneous MR-PET images are well fit.

Table 9. Result of neural networks learning (T2-weighted MRI and simultaneous MR-PET images)

	Sample	MSE	R
Training	12	2.49E-03	9.9962E-01
Validation	2	1.92E-02	9.0777E-01
Testing	2	1.57E-01	7.6643E-01

[Figure 22] is a graph showing regression.

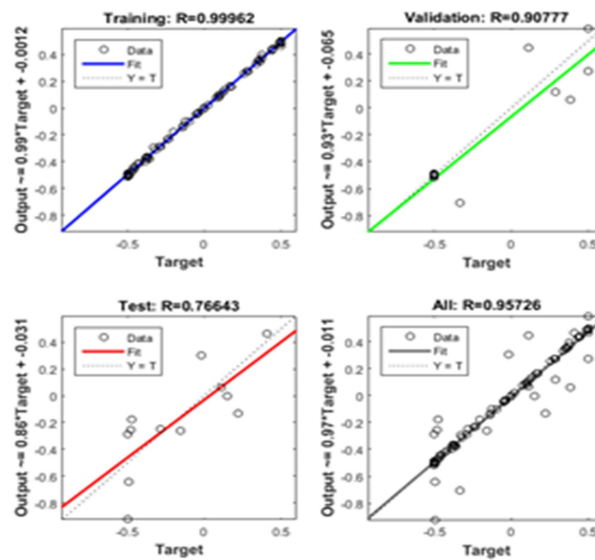


Figure 22. Regression graph (T2-weighted MRI and simultaneous MR-PET images)

## 2) Fitting degree of brain tumor PET image and simultaneous MR-PET images

[Figure 19] The Brain tumor-PET characteristic values in [Table 6] were input as input data of the neural networks. As target data, the simultaneous MR-PET (T2WI and Brain tumor-PET fusion image)

feature values in [Table 4] were input. [Table 10] shows that the R-value is close to 1 for both training, validation, and testing, indicating that the brain tumor-PET image and the simultaneous MR-PET image are well fit.

Table 10. Result of neural networks machine learning (brain tumor PET image and simultaneous MR-PET images)

	Sample	MSE	R
Training	12	2.49E-03	9.9969E-01
Validation	2	1.92E-02	9.8251E-01
Testing	2	1.57E-01	8.7602E-01

[Figure 23] is a graph showing regression.



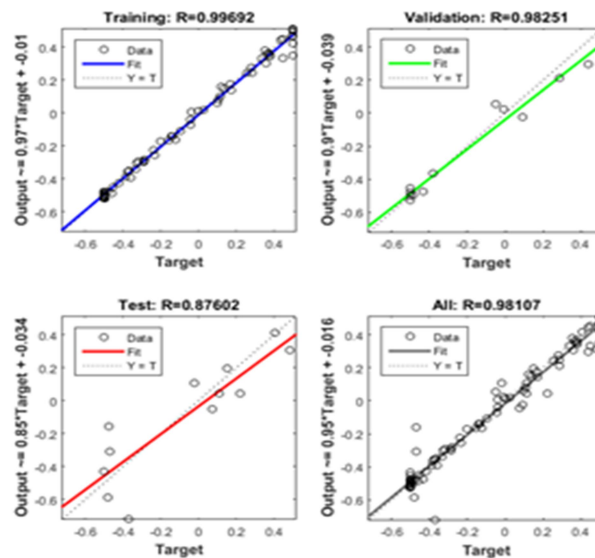


Figure 23. Regression graph (brain tumor PET image and simultaneous MR-PET images)

#### IV. Conclusion

With the advancement of science and technology, the era of the 4th industrial revolution is coming. In the medical field, the 4th industrial revolution has unified patient diagnosis and treatment, and the medical environment is rapidly changing from standardized evidence-based medicine to personalized precision medicine. The center of change in the medical environment is artificial intelligence (AI) technology. AI technology will be used in the entire 'before, middle, and after' process of diagnostic imaging equipment, such as CT, MRI, PET/CT, and simultaneous MR-PET, thereby providing a foundation for providing faster and more precise medical images. Simultaneous MR-PET, the state-of-the-art imaging device, significantly reduces radiation exposure (70% or more) compared with PET-CT, while the contrast of soft tissues is superior to that of PET-CT. If images are

scanned with sequential MR-PET equipment, a separate process of registration after saving each acquired image is required, and the possibility of errors cannot be ruled out. Simultaneous MR-PET is a device that simultaneously acquires and stores MR images and PET images in one session. In this paper, we tested and evaluated neural networks to ascertain how well the fusion images acquired by simultaneous MR-PET were mapped (fit degree) in the fused image of MRI and PET features. After pre-processing the experimental images at 256 X 256 pixels, the disease-like regions (regions with strong signals) were segmented with a threshold of 127. The segmented image was transformed into a 3-step 2D DWT to extract 6 X 16 feature values for each image. When comparing the extracted feature values for each image, we found that the low-frequency regions in the horizontal and vertical directions showed similar patterns, but the patterns were different in the high-frequency regions in the horizontal and vertical directions,

as well as the high-frequency regions in the diagonal direction. In particular, the signal values were large in the MRI T1 and T2 images.

The following results were obtained through neural network machine learning to analyze the degree of fitting.

1. Fitting degree of T1WI and simultaneous MR-PET images:

The regression (R) values were 0.984 for Training, 0.844 for Validation, and 0.886 for Testing.

2. Fitting degree of Dementia-PET and simultaneous MR-PET images:

The R values were 0.970 for Training, 0.803 for Validation, and 0.828 for Testing.

3. Fitting degree of T2-weighted MRI and simultaneous MR-PET images:

The R values were 0.999 for Training, 0.908 for Validation, and 0.766 for Testing.

4. Fitting degree of Brain tumor-PET and simultaneous MR-PET images:

The R values were 0.999 for Training, 0.983 for Validation, and 0.876 for Testing.

An R value closer to 1 is more appropriate; therefore, each image fused in the simultaneous MR-PET image verified in this study was suitable. However, it is necessary to continue research on images acquired with pulse sequences other than emphasis images in MRI images. These studies may help establish a useful protocol for the process of acquiring simultaneous MR-PET images.

#### Competing interests

The authors declare that there is no conflict of interest regarding the publication of this paper

#### [Acknowledgments]

This study was supported by the National Research Foundation of Korea (NRF) grant funded by the Korean government (MEST) (NRF-2020R111A1A01060851) and supported (in part) by research funds from Nambu University, 2020.

#### [References]

- [1] Peter K. Spiegel(1995), “The First Clinical X-Ray Made in America-100 Years”, *AJR*, Vol. 164, PP. 241~243.
- [2] G. Choi S, B. Lee(2014), “Application and Prospects of Molecular Imaging”, *Journal of the Korean Society of Radiology*, Vol. 8, No. 3, PP. 123–136.
- [3] Martin S Judenhofer, Hans F Wehrl, Danny F Newport, Ciprian Catana, Stefan B Siegel, Markus Becker, et al(2008), “Simultaneous PET-MRI: a new approach for functional and morphological imaging”, *Natural Medicine*, Vol. 14, PP. 459-465.
- [4] Heinz-Peter W. Schlemmer, Bernd J. Pichler, Matthias Schmand, et Al, “Simultaneous MR/PET Imaging of the Human Brain”, *Radiology*, Volume 248, Number 3, September 2008.
- [5] Yoon, Seok-Joo, Kim, Gwang-Jun, Jang, Chang-Soo(2012), “Classification of ECG arrhythmia using Discrete Cosine Transform, Discrete Wavelet Transform and Neural Network”, *The Journal of the Korea institute of electronic communication science*, Volume 7, Issue 4, PP. 727~732.
- [6] Lim, Jong-Myeong, Yoo, Ji-Sang(2012), “Super-resolution Algorithm using Discrete Wavelet Transform for Single-image”, *Journal of Broadcast Engineering*, Volume 17,

- Issue 2, PP. 344~353.
- [7] Cornelia B. Brendle, Holger Schmidt, Sabrina Fleisher, et al(2013), “Simultaneously Acquired MR/PET Images Compared with Sequential MR/PET and PET/CT : Alignment Quality”, *Radiology*, Vol. 268, No. 1, pp. 190~199
- [8] Park, Su A, Lee, Jun Hee, Kim, Wan Doo(2017), “Bio-fusion and Medical Device Industry”, *Transaction of the KSME C: Technology and Innovation*, Volume 5, Issue 1, PP 23~52.
- [9] Zaidi, Habib, Montandon, Marie-Louise(2006), “The New Challenges of Brain PET Imaging Technology”, *Current Medical imaging*, Volume 2, Number 1, pp. 3~13
- [10] Han, Dong-Kyun, Rhim, Jae-Dong, Lee, Jun-Haeng(2008), “Improvement in the Quality of Ultrasonographic Images Using Wavelet Conversion and a Boundary Detection Filter”, *Journal of the Korean Society of Radiology*, Volume 2, Issue 1, pp. 23~29.
- [11] Sang-Bock Lee(1999), “A Study on Recognition and Differential Compression of Disease Region in Medical Image”, Ph. D. Thesis, Cheongju University Press, Cheongju, Korea.
- [12] \_\_\_\_\_, “Draw a Kohonen SOM feature map?”, Internet : [tex.stackexchange.com/questions/144366/draw-a-kohonen-som-feature-map](https://tex.stackexchange.com/questions/144366/draw-a-kohonen-som-feature-map), Jan. 1, 2020. [Feb. 12, 2020]
- [13] Michel Haritopoulos, Hujun Yin, Nigel M. Allinson(2002), “Image denoising using self-organizing map-based nonlinear independent component analysis”, *Neural Networks*, Volume 15, Issue 8-9, pp. 1085~1098.
- [14] Yeochang Yoon, Sungduck Lee(2013.), “A Comparison of the Effects of Optimization Learning Rates using a Modified Learning Process for Generalized Neural Network”, *The Korean Journal of Applied Statistics*, Vol. 26, No. 5, PP. 847-856.
- [15] Suji Lee(2016), “A Study on Recurrent Neural Network Training Methods for Sequential Data Regression”, Master's Thesis, Seoul National University Graduate School Press, Seoul.

# Author Guidelines

Publishing your research content in ScholarGen Publishers. To help you to easily publish your manuscript and to ensure that you are aware of all the procedures of publishing, you are requested to go through our guidelines and detailed illustrations. Following illustrations will help you to understand the steps involved in publishing your manuscript in ScholarGen Publishers.

## Select a Journal

### How to select the journals?

The journal you wish to publish your article or manuscript should be on the similar subject line as that of your article. For example, “ScholarGen Publishers ” will accept articles on Life Science.

## Prepare your Manuscript

You need to follow few guidelines to ensure that your article is well written and well received by the scientific community and researchers.

## Plagiarism

According to the Merriam-Webster online dictionary, to “plagiarize” means:

- to steal and pass off (the ideas or words of another) as one’s own
- to use (another’s production) without crediting the source
- to commit literary theft
- to present as new and original an idea or product derived from an existing source

In other words, plagiarism is an act of fraud. It involves both stealing someone else’s work and lying about it afterward. Plagiarism is defined on delinquency in research as the stealing of another person’s ideas, tables, content, processes, results or words without citing the appropriate credit to be considered as crime. When it comes to plagiarism, content from the internet is equally comparable to information from appearing in a book or journal. ScholarGen Publishers does not encourage any form of plagiarism, thus we strongly recommend you to check your article content before you submit manuscript to any of our journals. Plagiarism can be checked through online plagiarism software tools (although they are not completely reliable) to minimize further complications.

## Formatting Prerequisites

### 1. Cover Letter

Cover letter must include the list of authors, and title of the manuscript. Mention the name of ScholarGen Publishers and choice of interest to which the submission is sent. Cover letter should briefly communicate upon your study to previously published work. It should declare that the work is not published elsewhere. The article type should be mentioned (Research/ Review/ Short Communication/ Editorial/ Case Report/ Perspectives). Lists any suggested reviewers if any. Also, include current telephone and fax numbers, as well as postal and e-mail address of corresponding author to maintain communication.

Sample Cover Letter can be downloaded here: [Cover Letter](#)

### 2. File Types

Authors may submit their manuscript files in either of the mentioned formats like Word (as .doc or .docx). All the figures must be in either of gif/ tiff/ jpeg formats. The figure should be of high resolution and the figure legend word limit is 300 words.

If your manuscript is or will be in .doc format and contains equations, you must be following the instructions below to make sure that your equations are editable when the file enters production. We recommend you to use Math Type to create the equation.

### 3. Manuscript Organization

The following order remains same for all the article types except Abstract, Keywords remain mandatory for Research and Review. Word limits for Research/ Review/ Cases/ remain 5000 words where as for Short Communications/ Perspectives/ Editorials remain 1500 words. References cited are excluded in the word limit.

Order of Manuscript

- Title
- Abstract
- Keywords
- Abbreviations
- Introduction
- Materials and Methods (Research)
- Subheadings (Review and rest of the article types)
- Results and Discussion (Results for Research/ Discussion for rest of the article types)
- Conclusion
- Acknowledgements
- References

**Title:** The word limit of the title should not exceed 15 words. Title should be a proper description and relevant to the work provided. Font has to be set to Times New Roman Bold, Title case.

**Abstract:** Abstract should describe the main objectives of the study. It should be able to list out all the work briefly. Significance and the results of the study need to be precise briefly. Abstract ‘word limit’ should be limited to 300 words.

Note: Abstracts should be free of citations.

**Keywords:** The major keywords used in the study need to be mentioned. Keywords limit is not more than 7-10 words.

**Abbreviations:** If any abbreviations are used in the study, their first usage has to be mentioned in full form along with the usage abbreviation in brackets. If there are too many abbreviations they have to be mentioned below the keywords.

**Introduction:** Introduction should be able to provide the background of the study. It should also provide comprehensive insight on the purpose of the study and its significance. Introduction needs to be descriptive and citations need to be provided.

**Materials and Methods:** Particular details and/or practices for new approaches have to be mentioned. For the used protocols the proper citations has to be mentioned. Results have to be unique and not copied from any other sources. This section should present enough detail to permit researchers to fully replicate your study. We recommend authors to put forward detailed protocols for less well-established methods.

**Results and Discussions:** This section might be further divided in subdivisions. Results and discussions must be providing the results. Illustrate the results of the experiments, the interpretation of these results, and the conclusions.

**Conclusion:** Authors should elucidate how the results communicate to the theory presented as the basis of the study and provide a concise explanation of the allegation of the findings.

**Acknowledgements:** Authors need to provide the funding details and the grant numbers if any. They might acknowledge their supported work.

**References:** Authors need to provide the references used in the text. All the references should be clearly mentioned along with the names, years, title of the article, volume number and page number.

### **Submit Manuscript**

Completed manuscript can be submitted at Submit Manuscript tab for the chosen Journal page.

### **Peer Review of Manuscript**

Peer review is scrutinizing process where an article or a manuscript is scrutinized by members who are specialized in their field. Every article is subjected to peer review before it is published in ScholarGen Publishers Journals except Editorials.

# **Scholargen Journal of Medical Imaging**

**Volume 03 Number 01 December 2020**

**Copy right Scholargen Journal of Medical Imaging, All right reserved.**

**This is identical to the Creative Commons Attribution Non-Commercial Licence.**

**Published on December 30, 2020**

**Subscription info : [office@scholargen.com](mailto:office@scholargen.com)**

**Open access on <https://scholargen.com/journals/journal-of-medical-imaging/>**



 ScholarGen Publishers

